AGU PUBLICATIONS

JGR

Journal of Geophysical Research: Oceans

RESEARCH ARTICLE

10.1002/2014JC010228

Key Points:
- The role of tidal pumping is comprehensively revealed by removing two effects
- Responses of ETM to river discharge and sediment settling velocity are explained

Correspondence to:
Q. Yu,
qianyu.nju@gmail.com

Citation:
Yu, Q., Y. Wang, J. Gao, S. Gao, and B. Flemming (2014), Turbidity maximum formation in a well-mixed macrotidal estuary: The role of tidal pumping, *J. Geophys. Res. Oceans*, *119*, 7705–7724, doi:10.1002/2014JC010228.

Received 10 JUN 2014
Accepted 15 OCT 2014
Accepted article online 20 OCT 2014
Published online 19 NOV 2014

Turbidity maximum formation in a well-mixed macrotidal estuary: The role of tidal pumping

Qian Yu[1,2], Yunwei Wang[1,2], Jianhua Gao[1], Shu Gao[1], and Burg Flemming[3]

[1]MOE Laboratory for Coast and Island Development, Nanjing University, Nanjing, China, [2]Faculty of Civil Engineering and Geosciences, Delft University of Technology, Delft, Netherlands, [3]Senckenberg Institute, Wilhelmshaven, Germany

Abstract Traditionally, vertical circulation (induced by gravity circulation and tidal straining), tidal pumping, and resuspension are suggested as the major processes for the formation and maintenance of the estuarine turbidity maximum (ETM). Due to strong mixing, tidal pumping is considered as the dominating process in macrotidal estuaries. To analyze field observation data, the classical empirical decomposition method is commonly suggested, but the tidal pumping flux (TPF) based on this method may lead to erroneous conclusions about the mechanisms of ETM formation because the effects of advection induced by the horizontal SSC gradient and fine bed sediment supply are ignored. If these effects are included, the TPF clearly reproduces the convergence patterns and thus demonstrates its role in the formation of the ETM. By a simplified analytical solution, the TPF is the result of the competition between the downstream flux induced by the river current together with the lag in sediment response and the upstream flux induced by tidal asymmetry and the lag. Field observations in the well-mixed macrotidal Yalu River estuary (located between China and North Korea) were analyzed. Tidal pumping is identified as the dominant mechanism of its ETM formation, and the position of the ETM for different river discharges and sediment settling velocities can be predicted by the concept of tidal pumping by numerical and analytical procedures. The present study provides a typical example of how to evaluate the tidal pumping contributions on ETM formation using the combined information provided by field data, numerical modeling results, and analytical solutions.

1. Introduction

Estuaries are key nodes of land-ocean interaction, the associated suspended sediment processes being crucial for global and regional material fluxes and environmental health [*Jay et al*., 1997; *Elliott and Whitfield*, 2011; *Blair and Aller*, 2012]. Within estuaries, there is commonly a reach where the water turbidity is markedly higher than both landward and seaward. This elevated suspended sediment concentration (SSC) is termed the estuarine turbidity maximum (ETM). The ETM has important influences on harbor siltation [*de Nijs et al*., 2009], ecological conservation [*Islam et al*., 2006], and biogeochemical dynamics [*Herman and Heip*, 1999; *Garnier et al*., 2010]. The understanding and prediction of ETM formation and variation are thus based on both theoretical and practical considerations.

Vertical circulation, tidal pumping, and resuspension are suggested as the major mechanisms for ETM formation [*Dyer*, 1997]. Vertical circulation can be generated by gravitational circulation and tidal straining [*Jay and Musiak*, 1994; *Burchard and Hetland*, 2010], the former being induced by the seaward barotropic pressure gradient and the landward baroclinic pressure gradient [*Pritchard*, 1956], the latter being due to enhanced vertical mixing during the flood and suppressed mixing during the ebb phase [*Simpson et al*., 1990]. As SSC is higher near the bed, the circulation pattern characterized by an up-estuary directed residual flow near the bottom, and a down-estuary flow near the surface, results in a net landward directed suspended sediment transport, which (at some point) encounters the seaward directed river transport to form the ETM [*Postma*, 1967; *Festa and Hansen*, 1976; *Burchard and Baumert*, 1998].

Tidal pumping denotes the barotropic, tide-induced suspended sediment transport. It is considered to be mainly caused by current asymmetry and sediment lag effects [*Uncles and Stephen*, 1989; *Dyer*, 1997; *Brenon and Le Hir*, 1999]. Because the up and down-estuary flows respond to different tidal conditions, the associated pumping fluxes converge at some point, at which the ETM is then induced. Especially in well-mixed

© 2014. American Geophysical Union. All Rights Reserved.

water bodies, tidal pumping plays a primary role in ETM formation, this feature having been revealed by various observational and numerical modeling approaches [*Allen et al*., 1980; *Uncles and Stephen*, 1989; *Le Hir et al*., 2001].

Numerous studies have shown that the ETM generally coincides with a muddy zone in the estuary (other parts of the estuarine bed being sandy or gravelly), and without tidal resuspension of muddy bed sediment, the ETM would either not exist or be significantly weaker [*Allen et al*., 1980; *Wellershaus*, 1981; *Uncle and Stephens*, 1993; *Sanford et al*., 2001]. However, a more important question is how the muddy zone is formed as such. *Allen et al*. [1980] pointed out that the mud reach and its associated ETM are essentially maintained either by tidal pumping and/or by vertical circulation.

Based on the field observational data, the vertical circulation can easily be recognized from velocity profiles, but the contribution by tidal pumping is relatively difficult to measure because it is the result of current and sediment transport interactions. A practical method to assess the effect of tidal pumping is the so-called decomposition method [*Dyer*, 1997]. In this procedure, the suspended sediment flux averaged over a tidal cycle is quantified as follows:

$$F = \frac{1}{T}\int_0^T \int_0^H U \cdot c \cdot dz \cdot dt$$
$$= \underbrace{c_0 u_0 H_0}_{F1} + \underbrace{c_0 \overline{u_t H_t}}_{F2} + \underbrace{u_0 \overline{H_t c_t}}_{F3} + \underbrace{H_0 \overline{u_t c_t}}_{F4} + \underbrace{\overline{c_t u_t H_t}}_{F5} + \underbrace{H_0 < \overline{u}_d \overline{c}_d >}_{F6} + \underbrace{H_0 < \overline{u_{dt} c_{dt}} >}_{F7} \tag{1}$$

where c is the SSC, u is the current velocity, T is the tidal period, H is the water depth, the subscript 0 denoting the mean value over time and space, the subscript t the vertically averaged tidal variation, the subscript d the deviations from the vertical means, and the subscript dt the temporal deviations from the tidally averaged deviations from the vertical means. Angled brackets ($< >$) and overbars ($-$) signify the means over the depth and the tidal cycle, respectively. $F1$ through $F7$ represent the individual components to be resolved in the decomposition procedure.

Each decomposed term represents a particular contribution related to a certain physical process [*Dyer*, 1997]. The first two terms ($F1$, $F2$) denote the residual flow of water and the tidally and vertically averaged SSC to provide the advective sediment flux (the Lagrangian flux). The terms $F3$ to $F5$ are the tidal pumping terms that are produced by the phase differences between the depth-averaged SSC, the depth-averaged velocity, and the tidal elevation. The last two terms ($F6$, $F7$) arise from the vertical circulation effects. This decomposition method has been applied widely in studies of sediment flux patterns and ETM formation mechanisms [*Winterwerp*, 1983; *Uncles et al*., 1985a, 1985b; *Su and Wang*, 1986; *Barua et al*., 1994; *Pino et al*., 1994; *Li and Chen*, 1998; *Ganju et al*., 2005; *de Nijs et al*., 2009, 2010; *Erikson et al*., 2013].

However, the analytical study of *Yu et al*. [2012a] has shown that the above tidal pumping flux (TPF) is also controlled by the horizontal SSC gradient. Because of the positive gradient upstream and the negative gradient downstream of it, the ETM may substantially affect the TPF. The fine sediment supply from the bed is also considered to be an important factor influencing both the SSC and the TPF [*van Leussen*, 1991; *Bass et al*., 2002]. The TPF, therefore, has different responses to the same hydrodynamic conditions over the mud zone at the ETM, on the one hand, and over the sand or gravel beds outside the ETM, on the other. This situation imposes a degree of circular argumentation, in that the TPF is used to investigate the ETM formation but, at the same time, is also influenced by the ETM itself; this association could ultimately confuse the judgment of the role of tidal pumping. Thus, in order to understand the role of tidal pumping correctly, a particular evaluation procedure must be followed, which is ideally based on both field observations and modeling. Furthermore, after establishing its dominant role, it should be possible to predict the position of the ETM on the basis of the tidal pumping effects.

The present study takes the macrotidal Yalu estuary, China, as an example, using field observations together with one-point numerical modeling and two-dimensional depth-averaged (2-DH) modeling to investigate the role of tidal pumping on ETM formation. The aims of the study are (a) to demonstrate the failure of the traditional decomposition method to identify the contribution of tidal pumping, (b) to introduce a new procedure by which the contribution of tidal pumping can be quantified, and (c) to show that the influence of river discharge and sediment settling velocity on ETM migration can be uniformly explained by the analytical expressions of TPF defined in *Yu et al*. [2012a].

© 2014. American Geophysical Union. All Rights Reserved.

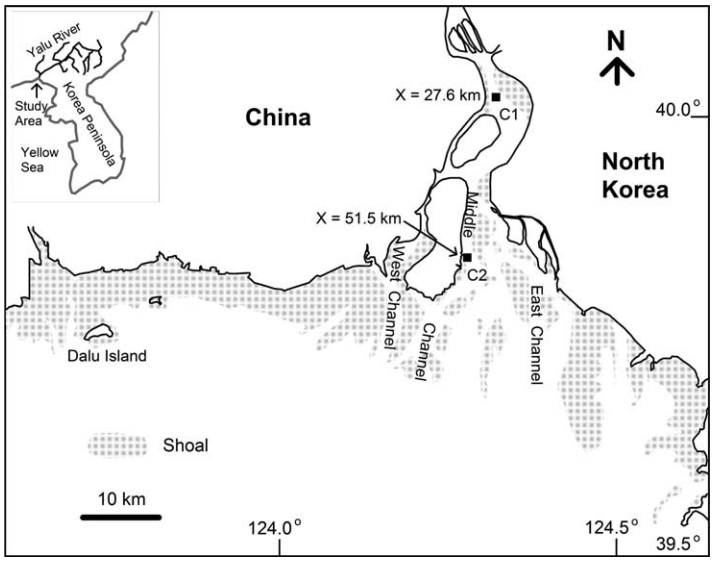

Figure 1. Map of the Yalu River estuary and the locations of the field observation stations C1 and C2. X is the distance from the upstream tidal limit. The survey of the longitudinal profile was carried out along the Middle Channel (the main channel).

2. Study Area

The Yalu River, which forms the border between China and North Korea, has a length of 790 km and discharges into the North Yellow Sea (Figure 1). Average water and sediment discharges over the last half century are about 2.5×10^{10} m^3/yr (or 800 m^3/s) and 1.6×10^6 t/yr, respectively [*Shi et al.*, 2013]. The hydrology of the river shows strong seasonal variations, and the well-defined wet season from June to September contributes 33% of the yearly water discharge and 80% of the yearly sediment load. The peak monthly averaged water discharge for August is about 1400 m^3/s, the reduced dry season water discharge being 600 m^3/s.

The Yalu River estuary is a macrotidal environment with a mean tidal range of 4.6 m. The semidiurnal tides are characterized by strong tidal currents (up to 1.5–2 m/s), the tidal limit being located 60 km upstream from the estuary mouth. As the average significant wave height outside the estuary near the Dalu Island (cf. Figure 1) is 0.5 m, wave action within the estuary is very limited. At the mouth, the river splits up into three channels lined by shoals, the middle channel being the main passage for water and suspended sediment exchange [*State Oceanic Administration*, 1998]. The ETM covers a 10–20 km stretch located between Km 30 and Km 60 from the upstream tidal limit where the SSC is almost zero. Within the ETM, maximum SSC values reach 1 kg/m^3, being an order of magnitude higher than in the waters up and downstream of it. The bed sediment mostly consists of sand, except for a mud reach coinciding with the ETM [*Gao et al.*, 2012].

3. Methods

3.1. Field Observation

Two field observation campaigns were carried out in the wet season of 1994 (12–18 August) and the dry season of 1996 (2–7 May), respectively [*Gao et al.*, 2004]. At ship-based anchor stations C1 and C2 (Figure 1), vertical profiles of current velocity, turbidity, and salinity were measured on an hourly basis over 25 h during both the 1994 and 1996 campaigns. The current velocity and salinity were measured by a direct-reading current meter and a CTD, respectively, and the turbidity was recorded with a Partech transmissometer. The measured turbidity was calibrated by in situ filtered water samples to allow conversion into SSC. In the 1994 campaign, the water column was measured at the surface, at 0.2, 0.4, 0.6, and 0.8H, as well as at the bottom (H being the water depth) from 12 to 13 August at station C1 (94C1) and from 11 to 12 August at station C2 (94C2) during intermediate tidal conditions (from spring toward neap). In 1996, all measurements were recorded at 0.5 m intervals within the water column to enhance the vertical resolution of the data sets, from 2 to 3 May at station C1 (96C1) and from 4 to 5 May at station C2 (96C2) during spring tide conditions.

In addition, longitudinal profiles through the water column were surveyed along the Middle Channel (the main channel) during the two campaigns (Figure 1). Profiles 94–1 and 94–2 were surveyed during the ebb on 14 August 1994 and during the flood on 18 August 1994, respectively. In 1996, the surveys along Profiles 96–1 and 96–2 were undertaken on 7 May during the ebbing tide and on 6 May during the flooding tide, respectively. Along each profile, turbidity (SSC) and salinity were measured at 7–11 sites and 5–10 depth intervals. All the data are based on the Chinese specification of oceanography survey.

© 2014. American Geophysical Union. All Rights Reserved.

3.2. One-Point Numerical Modeling

The analysis of the field observations has shown that the system can be studied by means of a depth-averaged model. In a first step, a one-point model based on a depth-averaged one-dimensional (1-D) model designed to simulate the depth-averaged SSC variations has been applied [*Dronkers*, 1986; *Uncles and Stephens*, 1989; *Sanford and Halka*, 1993; *Bass et al.*, 2002; *Yu et al.*, 2012a]. This model is based on simple physics to reveal the mechanics of SSC variation.

The longitudinal 1-D depth-averaged suspended sediment transport model is defined as

$$\frac{\partial CH}{\partial t} = -\frac{\partial UCH}{\partial x} + \mathit{Resuspension} + \mathit{Deposition} \tag{2}$$

with C as the SSC and U as the current velocity, both being depth averaged, and H as the water depth. The horizontal diffusion term is neglected [*Bass et al.*, 2002; *Stanev et al.*, 2007]. The first term on the right-hand side (RHS) represents the contribution from horizontal advection. Simultaneous local resuspension and deposition are assumed [*Sanford and Halka*, 1993], and width variations in velocity and SSC have been suppressed for simplicity.

The resuspension rate due to tidal currents can be simply written as [*Friedrichs et al.*, 1998; *Cheng and Wilson*, 2008]:

$$\begin{aligned} \mathit{Resuspension} &= BU^2, \quad B = \frac{M\rho C_D}{\tau_{cr}} && \text{if Bed available mass} > 0 \\ &= 0 && \text{if Bed available mass} = 0 \end{aligned} \tag{3}$$

where M is an erosion constant, C_D is the drag coefficient applicable to the depth-averaged velocity, and τ_{cr} is the critical erosion shear stress. For the sake of simplicity, M, C_D, and τ_{cr} are assumed to be constant over time and in space. Coefficient B thus becomes a constant that represents the resuspension capacity.

The deposition rate is given by:

$$\mathit{Deposition} = W_s C_{bed} = kW_s C, \qquad k = \frac{C_{bed}}{C} \tag{4}$$

where W_s is the sediment setting velocity, and C_{bed} is the near-bed SSC. For the sake of simplicity, it is assumed that the settling velocity and the ratio between the near-bed SSC (C_{bed}) and the depth-averaged SSC are constant over time and in space. Coefficient k thus also becomes a constant.

Combining equations (2–4) with the continuity equation for flowing water:

$$\frac{\partial UH}{\partial x} = -\frac{\partial H}{\partial t} \tag{5}$$

a simple form of the continuity equation for suspended sediment is obtained:

$$\frac{\partial C}{\partial t} = -U\frac{\partial C}{\partial x} + \frac{B}{H}U^2 - \frac{kW_s}{H}C \tag{6}$$

In this equation, the temporal SSC variation is controlled by three basic processes, namely advection of a horizontal SSC gradient, local resuspension, and deposition. These are parameterized as the first, second, and the third terms on the RHS of the equation, respectively. For this purpose, the SSC time series at a fixed station can be solved by equation (6) with the observed initial C, U, and H, the estimated SSC gradient and available mass of erodible fine sediment, and the best fit parameters B and kW_s.

3.3. 2-DH Numerical Modeling

3.3.1. Model Description

In order to examine in detail how the ETM formed in the well-mixed Yalu River estuary, and what the influence of river discharge and sediment settling velocity was on the location of the ETM, a 2-DH process-based model (Delft3D software package) was used. Delft3D has been successfully utilized and validated in a variety of different coastal environments to simulate sediment transport and morphological changes on different time scales [e.g., *Temmerman et al.*, 2005; *Xie et al.*, 2009; *Yu et al.*, 2012b; *Erikson et al.*, 2013; *van Maren et al.*, 2014; *Wang et al.*, 2014].

© 2014. American Geophysical Union. All Rights Reserved.

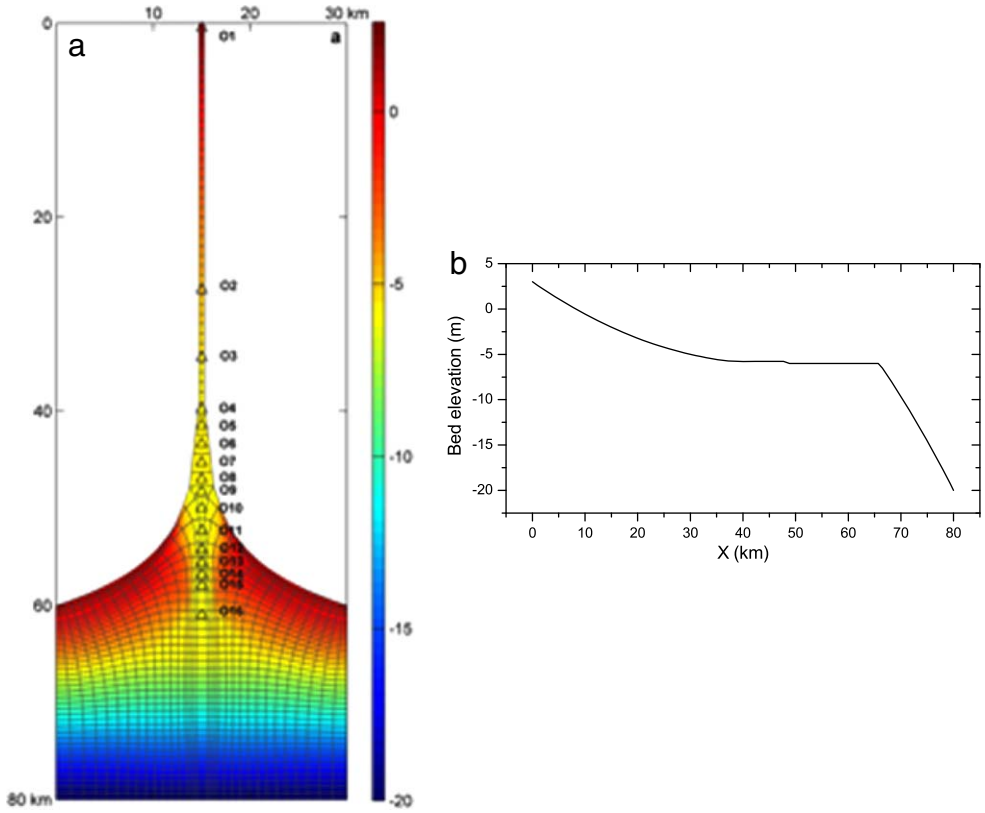

Figure 2. (a) The grid and bathymetry used in the 2-DH modeling exercise. A central channel is fringed by shallow shoals on either side. (b) Longitudinal bed elevation profile along the channel. The observation points within the channel are marked as O1 to O16. The color bar denotes bed elevation, and X is the distance from the upstream river boundary.

In accordance with the tide-dominated well-mixed characteristics and the model scale, only tidal forcing and river discharge were considered in the present case, vertical velocities, density differences, as well as wind and wave influences being neglected [*van der Wegen and Roelvink*, 2008; *Erikson et al.*, 2013; *van Maren et al.*, 2014]. The 2-DH continuity equation and nonlinear, shallow-water momentum equations for incompressible free surface flow are solved numerically with a constant seabed drag coefficient of 3×10^{-3} [*Soulsby*, 1997]. A minimum water depth of 10 cm was set for the requirement of numerical wetting and drying of the intertidal area. The detailed description of the Delft3D flow model can be found elsewhere [e.g., *Lesser et al.*, 2004].

Sediment transport is calculated by the van Rijn approach for cohesive materials [*van Rijn*, 2000]. Fine sediment erosion and deposition is calculated by the Ariathurai-Partheniades equation [*Partheniades*, 1965] and the simultaneous deposition model [*Sanford and Halka*, 1993], respectively. If the bed sediment thickness is less than a critical value (*Thresh*, threshold sediment thickness for transport and erosion), the erosion flux is reduced proportionally to the ratio of available sediment thickness over *Thresh*. The standard advection-diffusion equation is adopted for suspended sediment transport, and the Exner equation is employed to simulate the morphological changes based on the sediment mass conservation law.

3.3.2. Model Setting

A physics-based diagnostic 2-DH numerical model with simplified settings was chosen for the present study. Given that only principal characteristics of the Yalu River estuary are adopted and key processes of sediment transport are involved, the model is kept as simple as possible. Although certain details cannot be reproduced for a full comparison with real-world observations, the aim is to catch the first-order dynamics of ETM formation in this type of estuaries.

The schematized modeling geometry, grids, and bathymetry were constructed in terms of the physical characteristics of the Yalu River estuary (Figure 2). Upstream of the river/estuary boundary (at Km 40), the fluvial channel has a constant width of 500 m. From X = 40 km to X = 60 km (X being the distance from the upstream river boundary), the width increases rapidly seaward at an exponential rate to 30 km, this funnel-

© 2014. American Geophysical Union. All Rights Reserved.

Table 1. Parameter Settings for the One-Point Numerical Model

Observation	Estimated Position	Initial Bed Available Mass (kg/m^2)	$\partial_x C$ (kg/m^4)	B (kgs/m^4)	kWs (m/s)
94C1	Up-ETM	0	0 for H <= 5 m 1.43×10^{-5}H for H > 5 m	7.5×10^{-4}	1.6×10^{-3}
94C2	Within ETM	10	0	5.0×10^{-4}	1.0×10^{-3}
96C1	Up-ETM	0	0 for H <= 2.5 m 8.89×10^{-6}H for H > 2.5 m	7.5×10^{-4}	1.5×10^{-3}
96C2	Down-ETM	0	-6×10^{-5}	1.5×10^{-3}	1.0×10^{-3}

shaped geometry being common for tide-dominated estuaries [*Wells*, 1995]. The channel located in the middle of the estuary is fringed by shallow shoals on either side, its bed elevation decreasing from 3 m above sea level at the river boundary to −6 m at X = 66 km, from where it decreases linearly to −20 m at the sea boundary (Figure 2b). For orientation, the observation points within the channel are marked from O1 to O16. The highly schematized map and simple grid are representative of a typical tide-dominated estuary and, in a more universal sense, the modeling results therefore provide a generalized understanding of well-mixed estuarine sediment dynamics.

To fulfill the stability requirement, a numerical calculation time step of 1 min is prescribed. An erosion constant M of 5.0×10^{-4} kg m^{-2} s^{-1}, a sediment settling velocity of 1.25 mm/s, a critical shear stress for erosion of 0.25 N/m^2, and a sediment bulk density of 500 kg/m^3 were set for the mud transport calculation. It should be noted that the value for M is larger than that estimated in the one-point model ($B \approx 12M$, see Table 1), which is explained by the fact that the erosion equation in the one-point model (equation (3)) is simply proportional to the square of the current velocity, whereas in the 2-DH model the standard Ariathurai-Partheniades equation is adopted for the critical erosion shear stress. The sediment settling velocity is constant with the best fit values of the one-point model (Table 1, and $k \approx 1.0$–1.5). Considering the diagnostic nature of the model, the critical shear stress and sediment bulk density settings follow the classical estimates of *Whitehouse et al*. [2000]. The initial bed sediment has a constant thickness of 2 cm (10 kg/m^2), which is equal to the threshold sediment thickness for transport and erosion (*Thresh*).

The land and sea boundaries were forced by tidal and river discharge. For simplicity, only the main M2 tide was taken into account at the open sea boundary [*van der Wegen and Roelvink*, 2008; *Yu et al*., 2012b]. In accordance with observations, a uniform tidal range of 5.0 m across the entire width of the mouth (the open sea boundary) was chosen. At the sea boundary, dynamic equilibrium concentrations were defined for sediment transport [*Hibma et al*., 2003]. The inland open boundary was defined by a constant discharge of 800 m^3/s and a constant SSC of 0.06 kg/m^3, both corresponding to the average Yalu River discharge and SSC, respectively.

The model was at first run for 15 days with the whole set of equations while neglecting the sediment dynamics. After this initializing phase, a full model simulation, including sediment dynamics, was run for another 15 days to ensure that the SSC was able to reach stability.

In order to investigate the effects of river discharge and sediment settling velocity on the ETM dynamics, a sensitivity analysis was carried out with a typical wet season discharge of 1400 m^3/s and a typical dry season discharge of 650 m^3/s, and respective high and low settling velocities of 2.5 and 0.625 mm/s. Other settings were kept unchanged.

4. Results

4.1. Field Observation

The 25 h velocity, SSC, and salinity time series data are shown in Figure 3 for stations 94C1 and 94C2 and in Figure 4 for stations 96C1 and 96C2. The results indicate the well-mixed nature of the water body, suggesting that the system is well described by the depth-averaged data in both the wet and dry seasons. The results for the wet season are illustrated in Figure 5 and show that the ETM is developed upstream and slightly downstream of the C2 station along Profiles 94–1 and 94–2, respectively, the ETM being located upstream of the tip of salt intrusion. During the dry season, the ETM is formed between stations C1 and C2 (Figure 6), the cores of the ETM being associated with salinities of 3–5 psu for Profile 96–1 and of 1–2 psu for Profile 96–2.

© 2014. American Geophysical Union. All Rights Reserved.

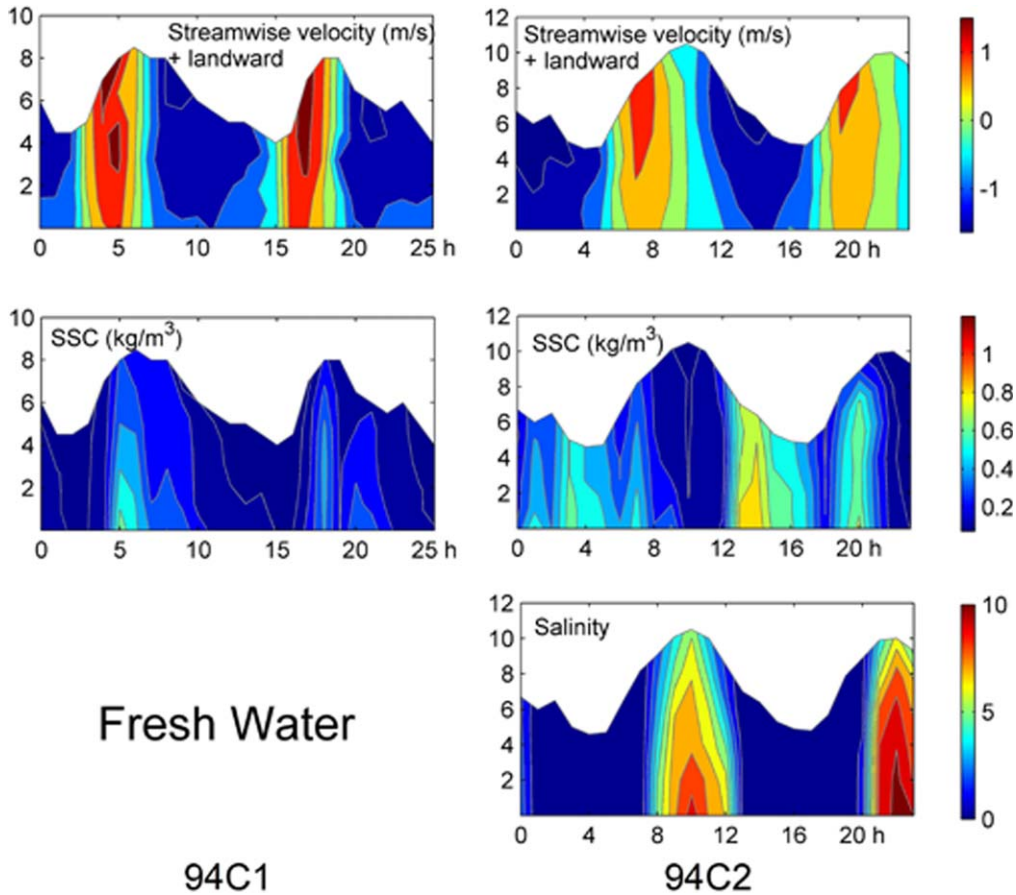

Figure 3. Vertical variations of current velocity, SSC, and salinity over two tidal cycles at stations C1 and C2 during the 1994 field campaign (wet season).

The estuarine mixing characteristics can be qualified by the Simpson number [*Simpson et al.*, 1990; *Becherer et al.*, 2011]:

$$Si = \frac{\overline{H}^2 \partial_x b}{u_*^2} \tag{7}$$

where the tidally averaged longitudinal buoyancy gradient $\partial_x b = g/\rho_0\, \partial_x \rho$ (ρ being the water density and ρ_0 the reference density of 1000 kg/m^3), $\overline{H}$ is the mean water depth, and $u^* = C_D^{1/2} U$ the scale for the bottom friction velocity, with the drag coefficient C_D corresponding to about 3.0×10^{-3} and U representing the tidal current velocity. Using the anchor and profile observations with $H \approx 6$ m, $\partial_x \rho \approx 10^{-3}$ (salinity increasing by 10 psu over 10 km along the channel), and $U \approx 1.4$ m/s, the Simpson number can be estimated as 6.0×10^{-2}. According to the upper boundary of 8.8×10^{-2} for the well-mixed stage [*Simpson et al.*, 1990], the Yalu River estuary can be classified as a well-mixed estuary.

Due to the well-mixed nature of the estuary, the anchor station observations can be represented by depth-averaged data (Figure 7). The 94C1 observations reveal a shorter flood period and a higher peak flood current speed, the ebb current being more stable around 1 m/s, which is due to the freshwater discharge during the wet season. The SSC shows a pattern with two peaks just before and after high water, the first peak being higher than the second one (Figure 7a). Figure 7b clearly shows that the flood and ebb phases at 94C2 are more symmetrical than those at 94C1, and that the SSC at the former station is higher and that the SSC peaks are correlated with the current speed peaks. In the case of the 1996 observations, the 96C1 situation is similar to that of 94C1 (Figure 7a), but the 96C2 situation differs markedly from the 94C2 one. Figure 7b shows that the SSC peaks now occurred before and after low water, the first peak again being higher than the second one. The suspended sediment flux was calculated by two methods: (a) by using the depth-averaged SSC,

© 2014. American Geophysical Union. All Rights Reserved.

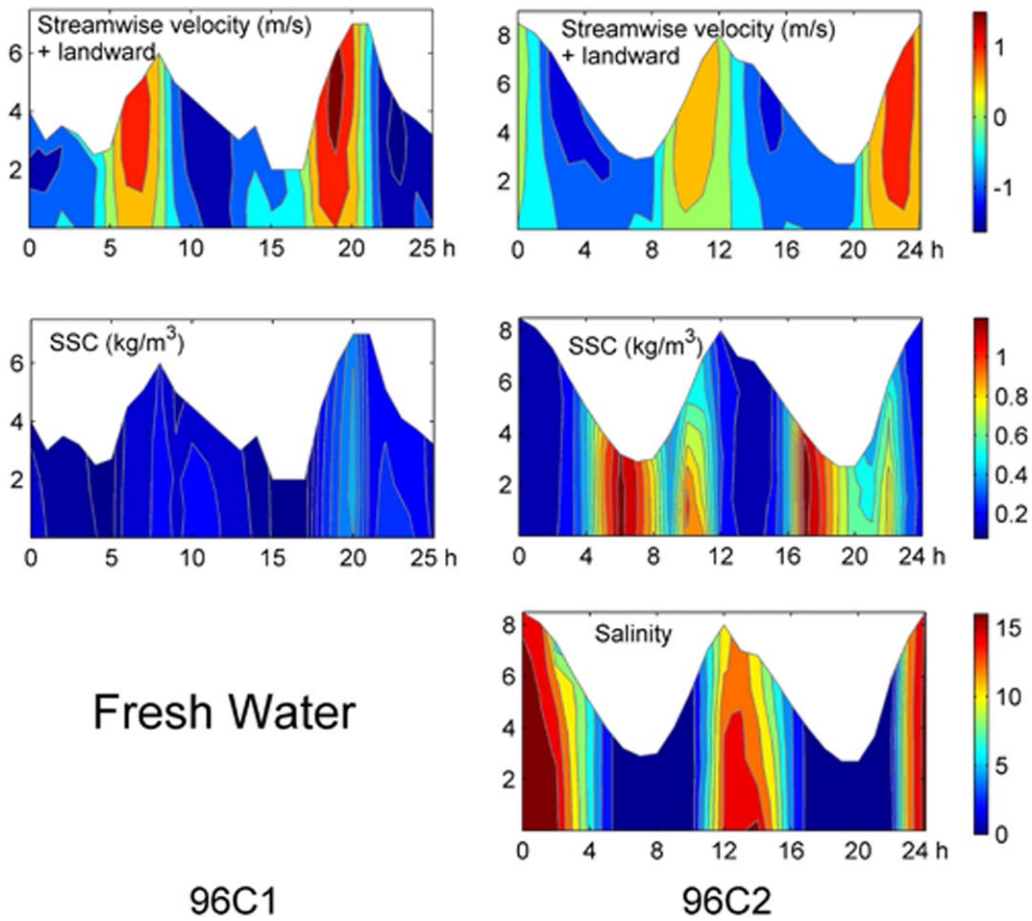

Figure 4. Vertical variations of current velocity, SSC, and salinity at stations C1 and C2 during the 1996 field campaign (dry season).

velocity, and water depth, and (b) by using a six-layer SSC, velocity, and water depth. The observations at all four station show little difference, implying that the contributions from vertical circulation are very limited and that the suspended sediment dynamics can be readily assessed by the depth-averaged model.

In order to investigate the controlling factors on SSC variation, the relationships between current speed, water depth, and SSC were analyzed (Figure 8). In the case of 94C1, the SSC is positively correlated with water depth, but the correlation with current speed is not very good. The SSC of 94C2, by contrast, is correlated with current speed rather than water depth. The SSC of 96C1 is similar to that of 94C1, but for 96C2, the SSC is negatively correlated with water depth and uncorrelated with current speed.

From the above results, some inferences on suspended sediment dynamics can be deduced. During the 1994 wet season, station C1 was located upstream of the ETM zone, and the water during flood had high suspended sediment concentrations, the SSC reaching its maximum value before high water. During high-water slack tide, part of the suspended sediment deposited, which resulted in a lowering of the SSC. At the onset of the ebb current, the previously deposited material was resuspended, causing the second peak just after high water. Because fine bed sediment supply is limited at this station, the SSC correlates with the water level rather than current speed. At station C2, by contrast, fine bed sediment supply is not limited, as a consequence of which a good correlation between SSC and current speed is observed, the higher SSC (in comparison with station C1) implying that station C2 was located within the ETM zone.

For the 1996 dry season, the SSCs at C1 are similar to those of 94C1, indicating that the sediment dynamic processes were identical. Station C2, on the other hand, was now located downstream of the ETM zone where fine bed sediment supply is limited. In this case, the ebb current carried turbid water to this station,

© 2014. American Geophysical Union. All Rights Reserved.

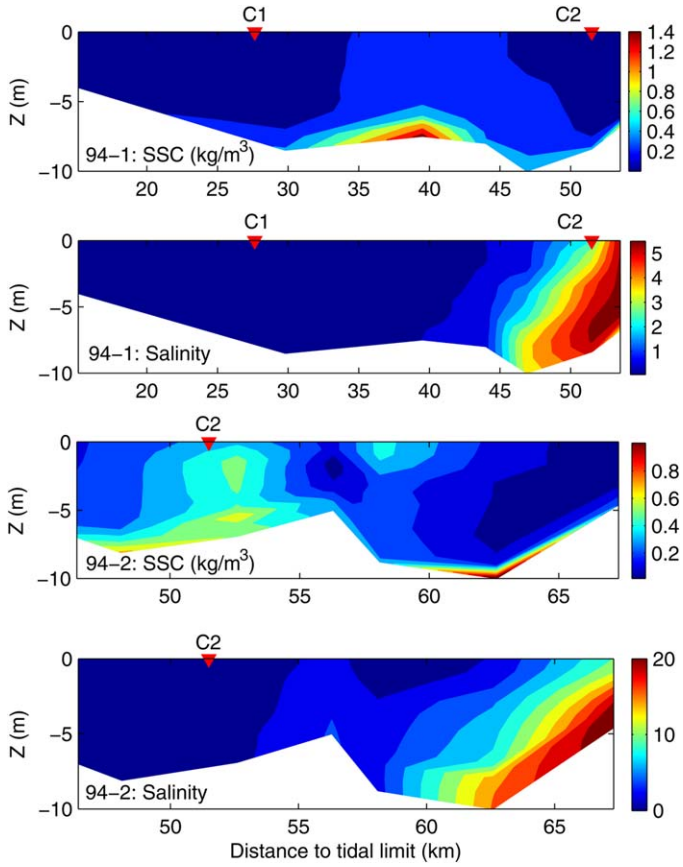

Figure 5. Vertical variations of salinity and SSC along the longitudinal profiles 94–1 and 94–2 during the 1994 field campaign (wet season), both the ship moving with the tide.

causing the two SSC peaks to occur around low water. The trends of the suspended sediment responses of 96C1 and 96C2 are practically mirror imaged due to their symmetrical position with respect to the ETM.

In summary, the circular processes of erosion, advection, and deposition of the ETM [e.g., *Grabemann and Krause*, 1989] can be identified: SSC peaks around high water if the station is located upstream of the ETM (C1) and around low water if the station is located downstream of the ETM (C2 in the dry season) and sediment from the ETM accumulates on the bed at C1 and C2, respectively.

The results of the longitudinal profile surveys (Figures 5 and 6) together with the above analysis of the anchor station data suggest that the ETM shifted from a position around station C2 during the 1994 wet season to a position between stations C1 and C2 during the 1996 dry season. This displacement is due to the different river discharge, the large discharge pushing the ETM downstream by a distance of about 10 km.

4.2. One-Point Numerical Modeling

The model is used to simulate the SSC variations of the data recorded at the four anchor stations, the results being shown in Figure 7. Beside the observed initial *C*, *U*, and *H*, the pending parameters are listed in Table 1 according to the field data analysis.

The longitudinal profile results of 1994 (Figure 5) suggest that the closer one gets to the ETM, the larger does the horizontal SSC gradient become. Thus, for the 94C1 observations, $\partial_x C$ is set to linearly increase from 0 at a water depth of 5 m (the smallest depth being 4.5 m) to 5×10^{-5} kg/m^4 at the largest water depth (8.5 m), the initial available mass of erodible fine bed sediment being zero, which is based on the primary knowledge that 94C1 is located upstream of the ETM where there is a lack of fine bed sediment supply. Station 94C2, by contrast, is located within the ETM where there is sufficient fine bed sediment, implying a zero SSC gradient and a large (10 kg/m^2) initial bed mud supply. The 96C1 observations have the same characteristics as those of 94C1, $\partial_x C$ being set to linearly increase from 0 at the smallest water depth (2.5 m) to 4×10^{-5} kg/m^4 at the largest water depth (7.0 m), the initial bed mud supply being zero. By contrast, a $\partial_x C$ value of -6×10^{-5} kg/m^4 and a zero initial bed mud supply are set for the 96C2 observations downstream of the ETM. The estimations of $\partial_x C$ and the initial bed mud mass can be examined by 2-DH numerical modeling.

Using typical values of 3.0×10^{-3} for C_D and 0.25 N/m^2 for τ_{cr}, the resuspension capacity *B* can be estimated by 12M. The best fit *B* values in Table 1 lie between 5.0×10^{-4} and 1.5×10^{-3}, which is consistent with the range of values from 2.0×10^{-5} to 3.5×10^{-3} kg m^{-2} s^{-1} for the erosion constant *M*. The values of *k* in equation (4) determined from the regression between the observed C_{bed} and *C* are 1.35 ($R^2 = 0.95$) for 94C1, 1.14 ($R^2 = 0.93$) for 94C2, 1.06 ($R^2 = 0.99$) for 96C1, and 1.03 ($R^2 = 0.98$) for 96C2. As a result, the coefficient *k* can be considered as a constant for the purpose of the present study, and the best fit values of $1.0–1.6 \times 10^{-3}$ for

© 2014. American Geophysical Union. All Rights Reserved.

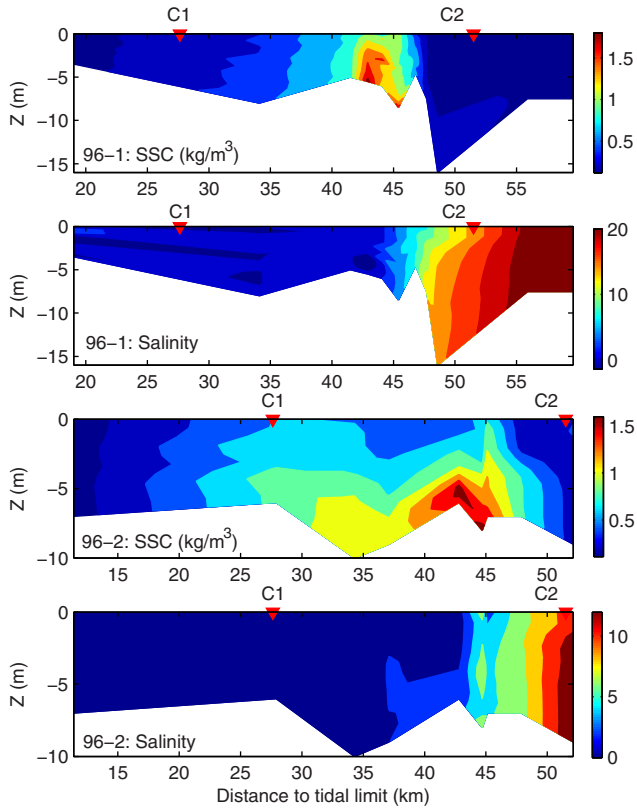

Figure 6. Vertical variations of salinity and SSC along the longitudinal profiles 96–1 and 96–2 during the 1996 field campaign (dry season), both the ship moving with the tide.

kW_s listed in Table 1 can hence be regarded as reasonable estimations of sediment floc settling velocity [*Winterwerp and van Kestern*, 2004].

In Figure 7, the modeled SSC time series are compared with the observations and the same circular processes of the ETM is revealed. The predictions suggest that the simple one-point model catches the key processes controlling the estuarine SSC variations quite well, including resuspension/deposition, horizontal advection, and bed sediment supply. The latter two are strongly influenced by the ETM, and the study of ETM formation should thus omit these processes.

4.3. 2-DH Numerical Modeling

The modeling time series of tidally averaged SSC at three observation points are shown in Figure 9. It indicates that the SSC indeed approaches stability after a 15 day run with sediment. Hereafter, the results are associated with the last tidal modeling period.

Observation points O4 (X = 39.8 km), O8 (X = 46.9 km), and O11 (X = 52.3 km) were chosen as typical estuarine locations representing the conditions upstream of the ETM, at the ETM, and downstream of the ETM, respectively. As can be seen from Figure 10, the modeling results compare well with the observations and the one-point modeling results of 94C1/96C1 (upstream of the ETM), 94C2 (ETM), and 96C2 (downstream of the ETM), respectively, indicating the circular processes of ETM.

For station O4 (upstream of the ETM), the modeled horizontal SSC gradient has a similar progression as the SSC, the former being more or less proportional to water depth, this method having been adopted in the one-point model. The range of the modeled gradient is between 0 and 7×10^{-5} kg/m^4, which is close to the estimated values for one-point modeling (Table 1). At station O8 (ETM), the SSC gradient varies from negative values around high water to positive ones around low water, which is due to the migration of the ETM. In the one-point modeling approach, a simple zero gradient was applied to represent a first order estimation. Station O11, located downstream of the ETM, the SSC gradient is inversely proportional to the SSC, the average value of about -5×10^{-5} kg/m^4 being comparable to the -6×10^{-5} kg/m^4 in the 96C2 modeling exercise.

The dynamics of the longitudinal distributions of the modeled streamwise velocity and SSC along the central channel are illustrated in Figure 11. In spite of the strong flood current soon after the onset of the flood phase (4.5 h), the SSC seaward of the ETM is low and relative uniform along the channel because of limited fine bed sediment availability. As the flood current crosses the mud reach, the turbidity increases with the development of the ETM (5.5 h, 6.5 h). The turbid water is then advected upstream (8.5 h) until the ebb phase begins (10 h). As the ETM moves downstream (11.5 h, 13 h), it is amplified to a peak value at 16 h because the strong ebb current reworks the muddy bed. The turbid water is now advected downstream until it eventually reaches the state at the beginning of the flood (17 h).

It should be noted that the upstream/downstream oscillation of the ETM is not symmetrical, the upstream migration (10 h) being more pronounced than the downstream one (17 h). In addition, the two SSC peaks around both high-water and low-water slack tide are not identical (Figures 10a and 10c), the ones upstream

© 2014. American Geophysical Union. All Rights Reserved.

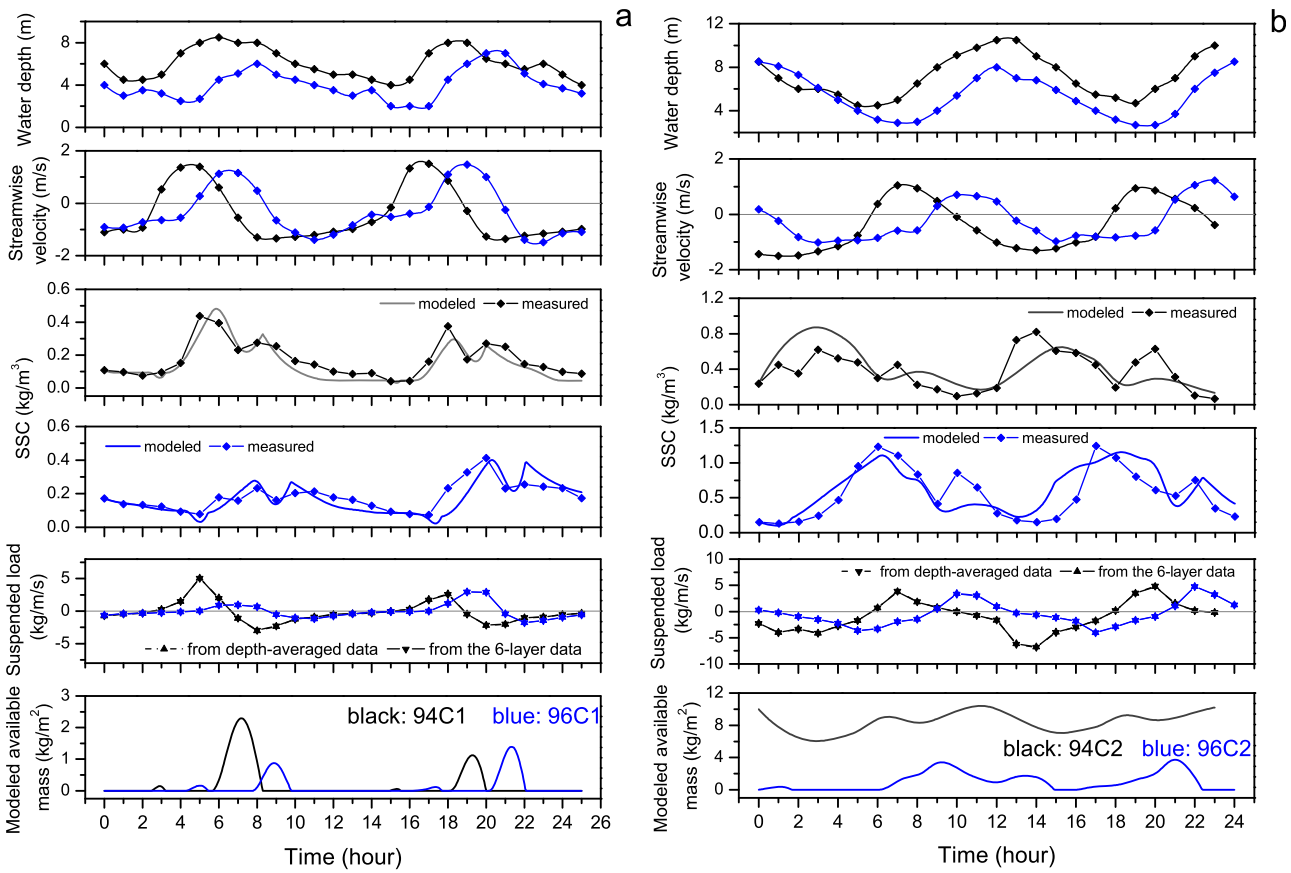

Figure 7. Variations in water depth, depth-averaged velocity, depth-averaged SSC, suspended sediment flux, and the one-point modeling results of SSC and available bed sediment mass over two tidal cycles based (positive values indicate the flood phase). The suspended sediment flux was calculated from the observed depth-averaged data and from the six-layer data. (a) Black and blue curves for 94C1 and 96C1 observations, respectively; (b) black and blue curves for 94C2 and 96C2 observations, respectively.

of the ETM being higher and narrower than the downstream ones, and the trough between the two upstream peaks being less pronounced than between the downstream one. The same characteristics are evident in the observational data (Figure 7). The difference in symmetry can be interpreted by the funnel shape of the estuary with its narrower upstream cross section [*Friedrichs et al.*, 1998].

Figure 12 shows the along-channel distribution of the tidal minimum mass of fine bed sediment, SSC, tidally averaged suspended sediment fluxes, as well as the longitudinal gradient (representing bed erosion/accumulation). The ETM can be identified between the observation points O4 and O11 by the elevated SSC and bed mud accumulation. At the initial state landward and seaward of point O8, the currents transport sediment downstream and upstream, respectively, causing net accumulation between O4 and O11 and erosion outside of this area. The fine bed sediment eroded both upstream and downstream thus converges on the middle section where the tidal resuspension processes form the ETM. The 2-DH modeling results confirm the important influence of both the ETM and the associated bed material distribution on the suspended sediment dynamics. As a consequence, the explanation of ETM formation should not be based on these interacting processes but pay more attention to the initial homogenous situation.

The results of the sensitivity analysis are shown in Figures 13 and 14. High river discharge pushes the ETM zone and the muddy bed reach downstream, the SSC peak moving from point O7 at 650 and 800 m^3/s discharge to O9/O10 at 1400 m^3/s discharge (Figure 13), which is consistent with the field observations. The lower SSC peak in the high discharge case is due to the large cross-sectional area in the mouth region of the estuary [*Friedrichs et al.*, 1998]. It should be noted that the SSC at the estuary/river boundary was kept the same in all three cases. With the decrease in sediment settling velocity the ETM zone migrates downstream, the SSC peak being located at O6/O7 for Ws = 2.5 mm/s, at O7 for Ws = 1.25 mm/s, and at O9 for Ws = 0.625 mm/s (Figure 14).

© 2014. American Geophysical Union. All Rights Reserved.

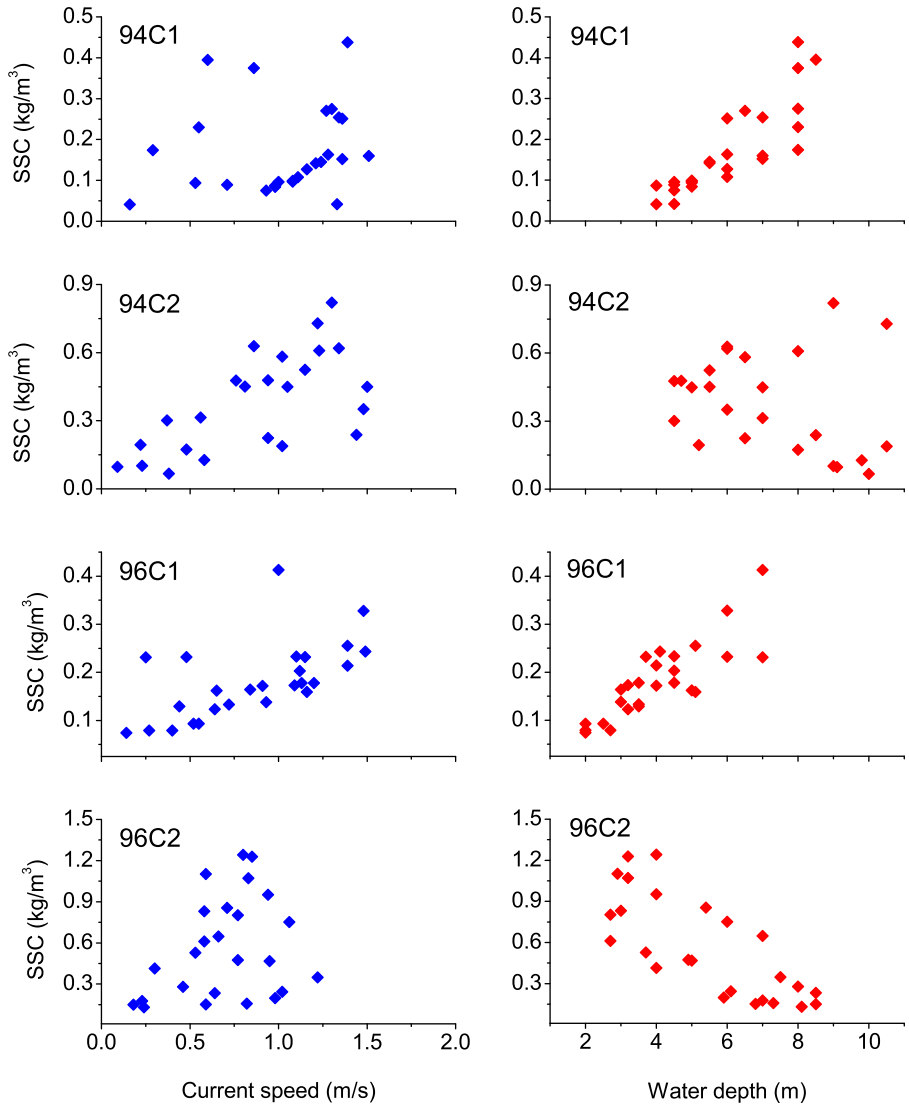

Figure 8. Relationship between (left) SSC and current speed and (right) SSC and water depth at the ship-based anchor stations.

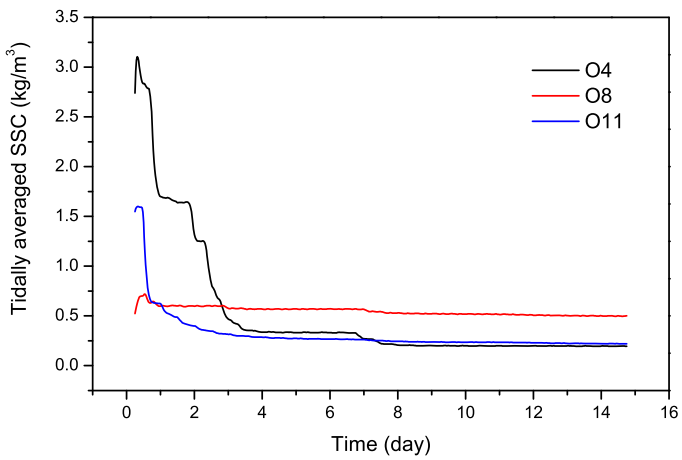

Figure 9. Time series of tidally averaged SSC at three observation points of the 2-DH modeling exercise, indicating that the SSC approaches stability after 15 days in the presence of bed sediment.

5. Discussion

5.1. The Role of Tidal Pumping on ETM Formation

The classical decomposition method of *Dyer* [1997] was adopted to study the sediment transport processes at the chosen anchor stations. The results in Table 2 indicate that the station upstream of the ETM (96C1) is characterized by a landward TPF, whereas the station downstream of the ETM (96C2) is associated with a seaward TPF, the net divergence destroying rather than forming an ETM. The method therefore negates any contribution by tidal pumping.

© 2014. American Geophysical Union. All Rights Reserved.

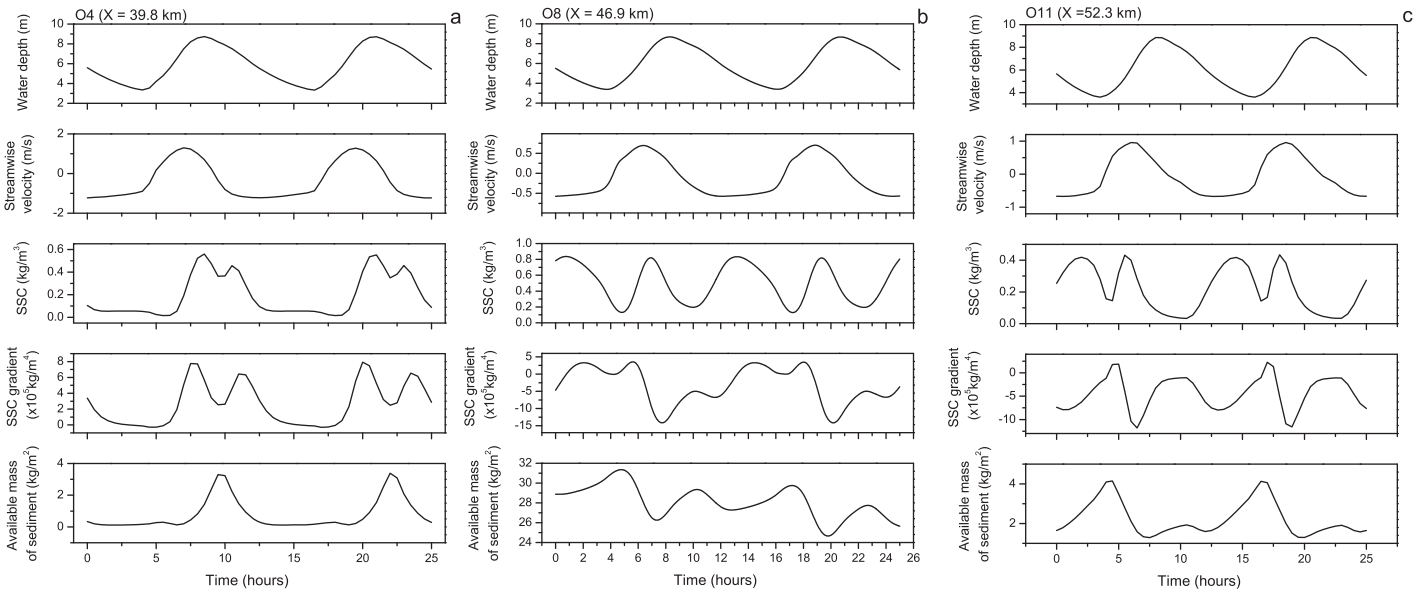

Figure 10. The 2-DH modeling results of water depth, streamwise velocity, SSC, horizontal SSC gradient, and available mass of fine bed sediment at observation point of (a) O4 (X = 39.8 km), (b) O8 (X = 46.9 km), and (c) O11 (X =52.3 km), which represent typical conditions upstream of the ETM, at the ETM, and downstream of the ETM, respectively. X is the distance from the upstream river boundary, and positive velocities indicate the flood current.

However, as shown in the present study, the TPF is strongly influenced by the advection induced by the horizontal SSC gradient and fine bed sediment supply. As a result, the inherent exclusion in the decomposition method of tidal pumping as a factor in estuarine sediment flux is highly questionable.

In order to assess the actual contribution of tidal pumping, the one-point model was run with new settings to remove the effects of advection and sediment supply (simulation 2 in Figure 15). Simulation 2 is a numerical experiment with sufficient mud at the bed and, negating advection effects, the SSC is only determined

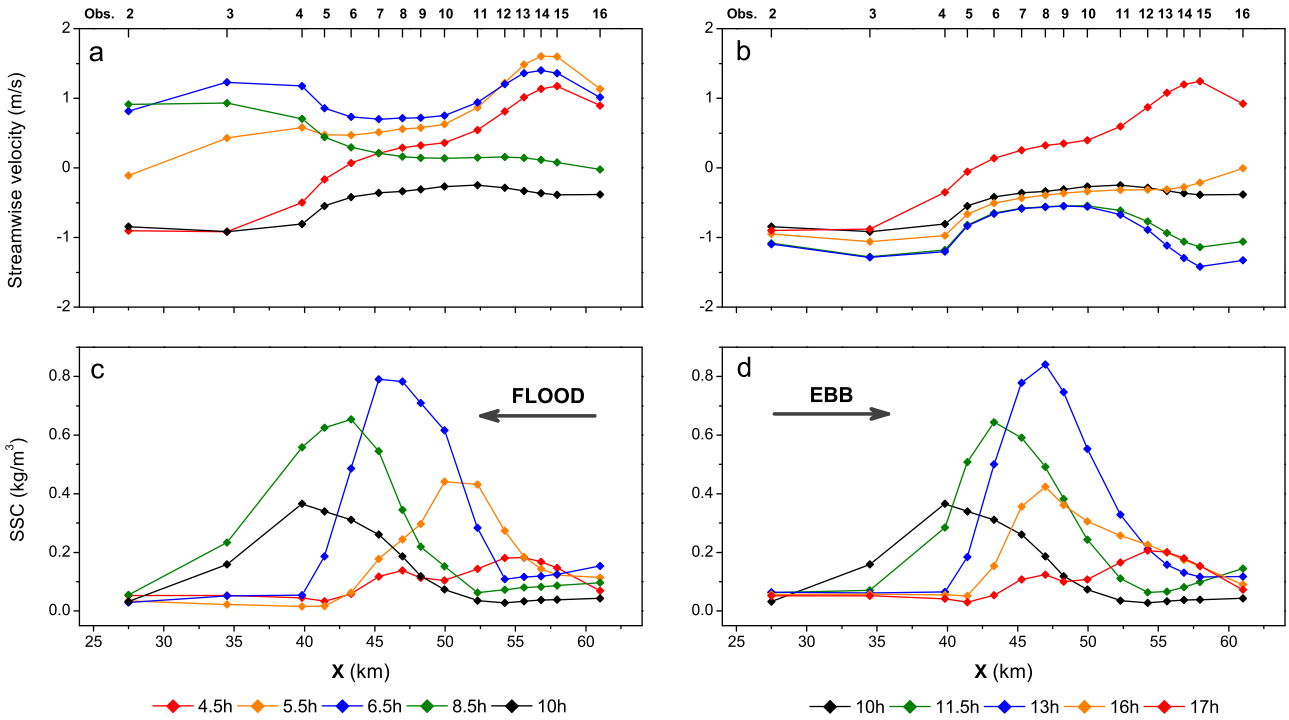

Figure 11. The 2-DH modeling results of the depth-averaged streamwise velocity and SSC along the channel at different tidal phases over a whole tidal cycle from the beginning of a flood phase (4.5 h) to the onset of the next flood phase (17 h).

© 2014. American Geophysical Union. All Rights Reserved.

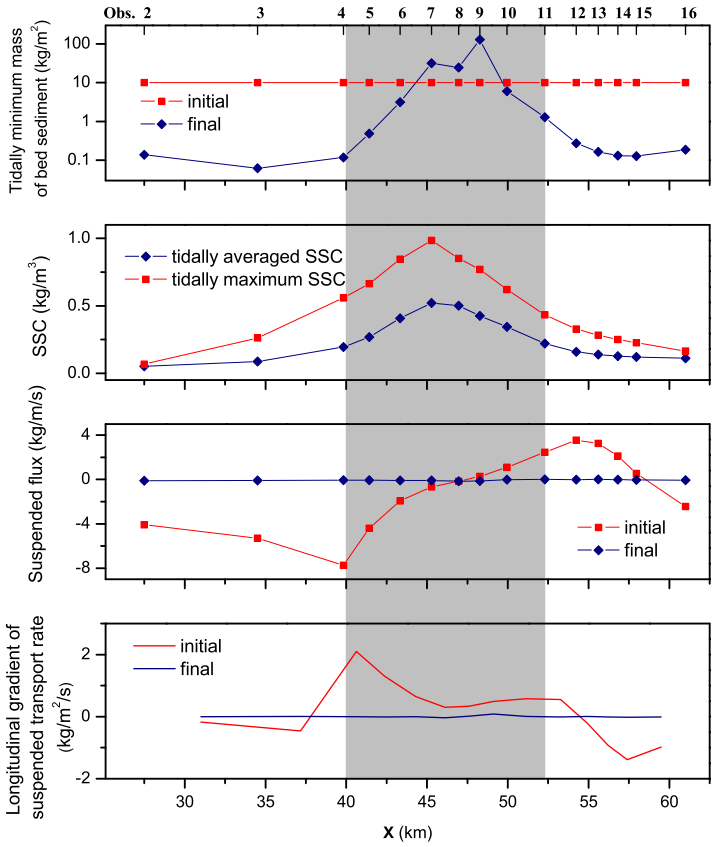

Figure 12. The 2-DH modeling results of the along-channel minimum mass of fine bed sediment, SSC, tidally averaged suspended sediment fluxes, and the longitudinal gradient of the latter (representing bed erosion/accumulation). The shadow area denotes the ETM zone.

by local erosion/sedimentation processes. The results are compared with those of the reference simulation 1, which was applied with zero initial bed mud and advection to fit the observations in Figure 7. The SSC time series and suspended sediment flux are shown in Figure 15, which reveals a large influence of both advection and local sediment supply. In Figure 16, the decomposed suspended sediment fluxes are confronted with those obtained in simulations 1 and 2. The original simulation 1 revealed a TPF deficit in the ETM zone, which agrees with the field observations. However, the decomposed fluxes in simulation 2 show a downstream TPF upstream of the ETM station and an upstream TPF downstream of the ETM station, this sediment flux convergence being clear evidence for ETM formation by tidal pumping.

In summary, to explain ETM formation, an initially homogenous spatial bed mud and SSC distribution should be assumed (ETM not being developed), at which time the TPF is only associated with tidally forced sediment transport. As shown, this results in high SSC and bed mud accumulation within a certain area—the reach associated with the formation of the ETM. Once the ETM has formed, the effects of sediment availability and advection can strongly influence the decomposition results based on the method of *Dyer* [1997], to the point of actually compensating the decomposed TPF. Thus, the classical decomposition method of ETM processes by *Dyer* [1997] involves the strong interferences of the effects of sediment availability and advection induced by horizontal SSC gradients for the TPF calculation, and can not correctly evaluate the role of tidal pumping on the ETM formation. As a consequence, the correct assessment of the tidal pumping contribution is only achieved by comparing the decomposed fluxes up and downstream of the ETM with the corresponding SSCs in which these effects have been removed.

It is estimated that, for an idealized stable case (e.g., the 2-DH modeling), when the steady equilibrium ETM has been formed, it is easy to find two cross estuarine sections located up and downstream of the ETM, which has the same tidal mean SSC. Based on the continuity, the total sediment flux and water flux are the same for these sections, and, due to the same tidal mean SSC, they have the same Lagrangian flux, suggesting the same TPF. However, the real estuarine sediment dynamics are influenced by the varied boundary conditions, including the spring-neap tidal variations, seasonal (wet-dry) river discharge variations, and also the decadal oscillations of bathymetry and estuarine shape [*Gelfenbaum*, 1983; *Schoellhamer*, 1996; *Grabemann et al.*, 1997]. The tidal pumping responses to these variations and move the ETM along the estuary. Therefore, the TPF at the above two sections may show different combinations, and the TPF deficit based on the relatively short-term (i.e., 25 h for fortnight) measurements (e.g., simulation 1 in Figure 15) does not sufficiently suggest the destruction of ETM, but rather than indicates the movement of ETM.

Although influences of vertical circulation and stratification can be neglected because of the well-mixed nature of the Yalu River estuary, the formation of the ETM may also be affected by some other factors such

© 2014. American Geophysical Union. All Rights Reserved.

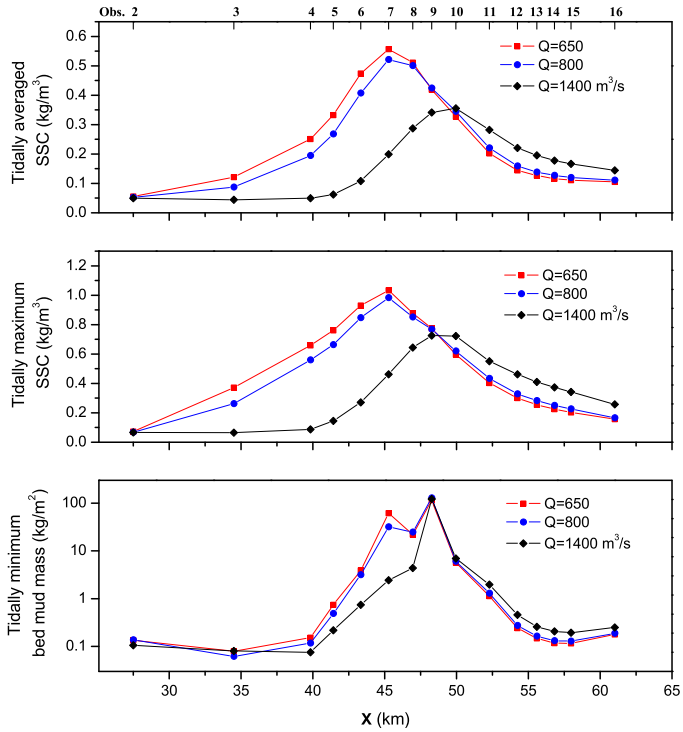

Figure 13. Sensitivity analysis of river discharge (Q) determined by 2-DH modeling. The 650, 800, and 1400 m^3/s discharges represent the dry season, average, and wet season, respectively.

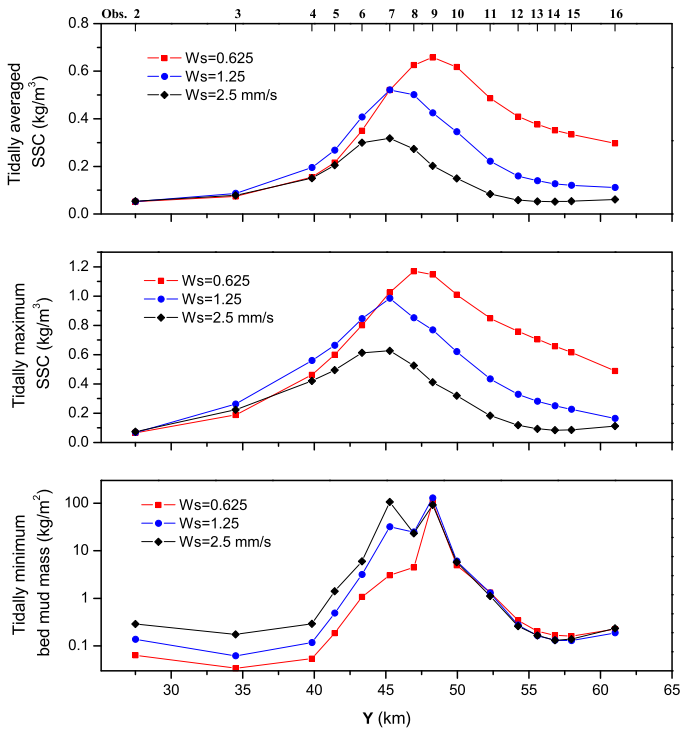

Figure 14. Sensitivity analysis of sediment settling velocity (Ws) determined by 2-DH modeling. The 0.625, 1.25, and 2.5 mm/s settling velocities represent low, middle, and high settling rates, respectively.

as lateral circulation [*Geyer et al.*, 1998; *Kim and Voulgaris*, 2008; *Gong et al.*, 2014], flocculation [*Xu et al.*, 2010; *Lefebvre et al.*, 2012; *Wang et al.*, 2013], and wave resuspension on shoal areas [*Green et al.*, 2000; *Jago et al.*, 2006]. Due to limited observational data, these effects are currently difficult to evaluate and should hence receive more attention in the future.

The present study, as a first step, focuses on the well-mixed (usually macrotidal) estuaries. For partially mixed mesotidal estuaries with pronounced baroclinic effects, the concept of the present study that removing the effects of sediment availability and advection has reference significance for the field and modeling data analysis, and the quantitatively separation and evaluation of the contributions of tidal pumping and vertical circulation are an interesting and challenging issue for the future research.

5.2. The Position of ETM Influenced by River Discharge and Sediment Settling Velocity

In the above section, a method to assess the tidal pumping contribution on ETM formation has been suggested. This procedure, however, does not identify the position of the ETM within the estuary. This can be achieved in a simple way by applying the analytical solution of suspended sediment flux for well-mixed water proposed by *Yu et al.* [2012a], which allows the identification of the location of sediment convergence as the point where the ETM develops.

It is well known that river discharge affects the ETM, high discharges pushing the ETM up to 10 km downstream [*Postma*, 1967; *Uncles and Stephen*, 1989; *Brenon and Le Hir*, 1999; *Kappenberg and Grabemann*, 2001]. Through numerical modeling approaches, *Brenon and Le Hir* [1999] and *Cheng et al.* [2013] have shown that the position of the ETM is also influenced by sediment

© 2014. American Geophysical Union. All Rights Reserved.

Table 2. Decomposed Tidally Averaged Suspended Sediment Fluxes per Unit Width in Terms of the Field Observations (kg/m/s), TPF = F3 + F4 + F5, Positive Being Landward

Observation	F1	F2	F3	F4	F5	TPF	F6 + F7	Total
94C1	−0.449	0.078	−0.057	0.172	0.069	0.184	0.008	−0.178
94C2	−1.156	0.392	0.108	−0.452	0.055	−0.289	0.007	−1.046
96C1	−0.239	0.095	−0.031	0.077	0.058	0.104	0.001	−0.038
96C2	−0.706	0.356	0.122	−0.271	0.097	−0.051	−0.012	−0.413

settling velocity, low settling velocities favoring the downstream movement of the ETM. These findings are also confirmed by the present 2-DH modeling results (Figures 13 and 14). Based on the present analysis, tidal pumping is mainly responsible for the ETM formation. The ETM migration induced by river discharge and sediment settling velocity should thus also be influenced by the tidal pumping processes. This issue is investigated below by applying the analytical solution of *Yu et al*. [2012a] to the 2-DH modeling results.

The analytical solutions for the decomposed suspended sediment fluxes (*F*1 to *F*5 in equation (1)) are provided by *Yu et al*. [2012a] under the assumption of a constant $\partial_x C$ and sufficient bed sediment supply. *F*4 is the result of temporal covariations of velocity and SSC (equation (1)), which has been suggested to be the most important part of the TPF. The solution of *F*4 has several zero and first-order trivial terms, which suggest a probable importance of *F*4 for the TPF, this having also been confirmed by field observations [e.g., *Su and Wang*, 1986; *Li and Chen*, 1998; *Ganju et al*., 2005], including those of the present study (cf. Table 2). *F*4 is thus considered to be the main part of the TPF. As advection effects can be excluded, the *F*4 solution is applied with zero $\partial_x C$:

$$F4 = K\widehat{F4} \qquad K = \frac{u_1^3 h_0}{2\sqrt{\omega^2+D^2}}\frac{B}{h_0}$$

$$\widehat{F4} = \underbrace{2\hat{u}_0\cos\theta_\omega}_{1} - \underbrace{\frac{1}{2}\hat{h}\cos(\phi-\varphi_1)\cos\theta_\omega}_{2} + \underbrace{\hat{u}_2\cos(2\varphi_1-\varphi_2+\theta_\omega)}_{3}$$
$$-\underbrace{\frac{1}{4}\hat{h}\cos(\phi-\varphi_1-\theta_\omega)}_{4} + \underbrace{\frac{\sqrt{(\omega/D)^2+1}}{2\sqrt{4(\omega/D)^2+1}}\hat{u}_2\cos(2\varphi_1-\varphi_2-\theta_{2\omega})}_{5} \tag{8}$$

$$\hat{u}_0 = u_0/u_1 \qquad \hat{u}_2 = u_2/u_1 \qquad \hat{h} = h/h_0 \qquad D = \frac{W_s C_{bed}}{CH}$$

where the *F*4 flux is expressed by the product of the characteristic value (*K*) and the nondimensional flux ($\widehat{F4}$), ω is the M2 tidal frequency, u_0 is the residual velocity, u_1 and u_2 are the depth-averaged amplitudes of the M2 and M4 velocities, respectively, φ_1, φ_2 are the phases of the M2 and M4 velocities, respectively, h_0 is the average water depth, and h and ϕ are the amplitudes and phases of the M2 tidal elevations, respectively. *B* is the resuspension capacity in equation (3), and *D* is the deposition capacity. The terms $\theta_\omega = \tan^{-1}\omega/D$ and $\theta_{2\omega} = \tan^{-1}2\omega/D$ represent the phase lag of SSC to the forcing factors in the M2 and M4 frequencies, respectively. Landward is denoted by the positive direction. A detailed description of the solution can be found in *Yu et al*. [2012a].

The longitudinal $\widehat{F4}$ distribution can be used to identify the convergence point of suspended sediment transport. At first, the harmonic analysis of the modeled velocity and water depth at the observation points O4 to O12 associated with discharges of 800 and 1400 m^3/s is carried out to provide the longitudinal distributions of u_0, u_1, u_2, φ_1, φ_2, h_0, h, ϕ. The deposition capacity *D* can be estimated by the mean depth of 6 m, the C_{bed}/C of 1.5, and the three sediment settling velocities derived from the 2-DH modeling. The ω/D can be estimated as 0.96, 0.48, and 0.24 for W_s of 0.625×10^{-3}, 1.25×10^{-3}, and 2.5×10^{-3} m/s, respectively. With these the phase lag θ_ω and $\theta_{2\omega}$ can be calculated.

In the next step, the five terms of $\widehat{F4}$ are evaluated using the characteristic values: 0.15 for $\hat{u}_0$, 0.3 for $\hat{u}_2$, 0.4 for $\hat{h}$, 0.4 for $\sqrt{(\omega/D)^2+1}/(2\sqrt{4(\omega/D)^2+1})$, 0.3 for $\cos(\phi-\varphi_1)$, 0.9 for $\cos\theta_\omega$, 1 for $\cos(2\varphi_1-\varphi_2+\theta_\omega)$, 0.2 for $\cos(\phi-\varphi_1-\theta_\omega)$, and 0.8 for $\cos(2\varphi_1-\varphi_2-\theta_{2\omega})$. The characteristic values are 0.27 for term 1, 0.054 for term 2, 0.3 for term 3, 0.02 for term 4, and 0.096 for term 5. As term 4 is very small, it can be neglected.

© 2014. American Geophysical Union. All Rights Reserved.

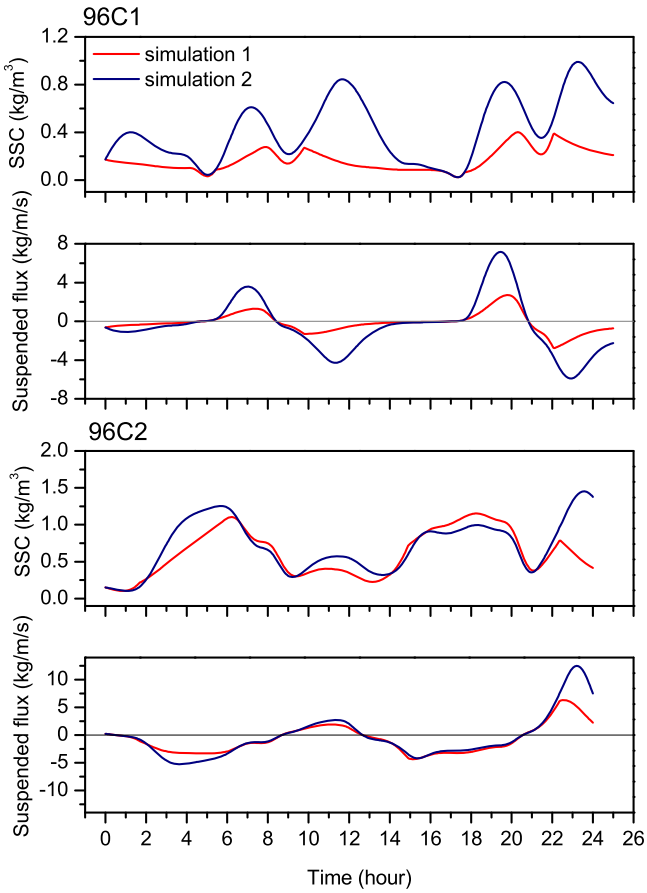

Figure 15. SSC and suspended sediment flux variations simulated by one-point modeling. Simulation 1 is the reference case, in association with the effects of advection induced by the horizontal SSC gradient and with zero initial fine bed sediment supply, to fit the observations represented in Figure 8. Simulation 2 is the numerical experiment with sufficient bed mud and ignoring advection effects, the SSC being only determined by local erosion/sedimentation processes.

Term 2, which is the result of interactions between the M2 depth-velocity phase difference and sediment response lag, is also small and can hence be neglected. The nondimensional *F*4 can hence be written:

$$\widehat{F4}=2\hat{u}_0\cos\theta_\omega+\hat{u}_2[\cos(2\varphi_1-\varphi_2+\theta_\omega)+0.4\cos(2\varphi_1-\varphi_2-\theta_{2\omega})] \tag{9}$$

The first term on the RHS is the sediment flux induced by the residual current and sediment response lag. Because of the downstream direction of the residual velocity, this term has a negative value. Along the estuary, the absolute values of the dimensionless residual velocity decrease markedly, implying a reduced downstream transport. The second term has a positive value, showing the importance of the tidal velocity asymmetry on the upstream transport. This term is determined by the tidal velocities and their phases combined with the sediment phase lag, both the phase lags to the M2 and the M4 forcing factors (θ_ω and $\theta_{2\omega}$) playing a role. This equation shows that tidal pumping can be simply viewed as the competition between the downstream river transport and the upstream transport induced by tidal asymmetry. It should be noted that the above two processes are affected by the sediment lag [*Yu et al.*, 2011].

Using the nearly constant along-stream value of 0.3 for $\hat{u}_2$, and the typical value of 0.9 for $\cos\theta_\omega$, the equation can be simplified to read:

$$\widehat{F4}=1.8\hat{u}_0+0.3[\cos(2\varphi_1-\varphi_2+\theta_\omega)+0.4\cos(2\varphi_1-\varphi_2-\theta_{2\omega})] \tag{10}$$

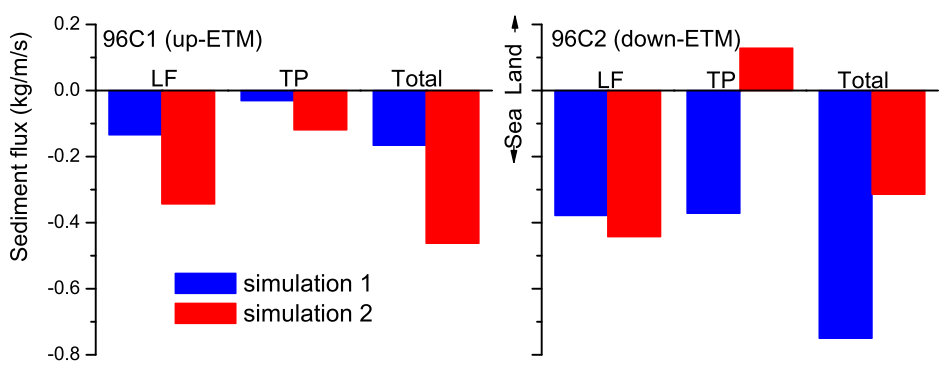

Figure 16. The decomposed tidally averaged suspended sediment fluxes per unit width (kg/m/s), LF and TP denoting Lagrangian flux (F1 + F2) and tidal pumping (F3 + F4 + F5), respectively.

© 2014. American Geophysical Union. All Rights Reserved.

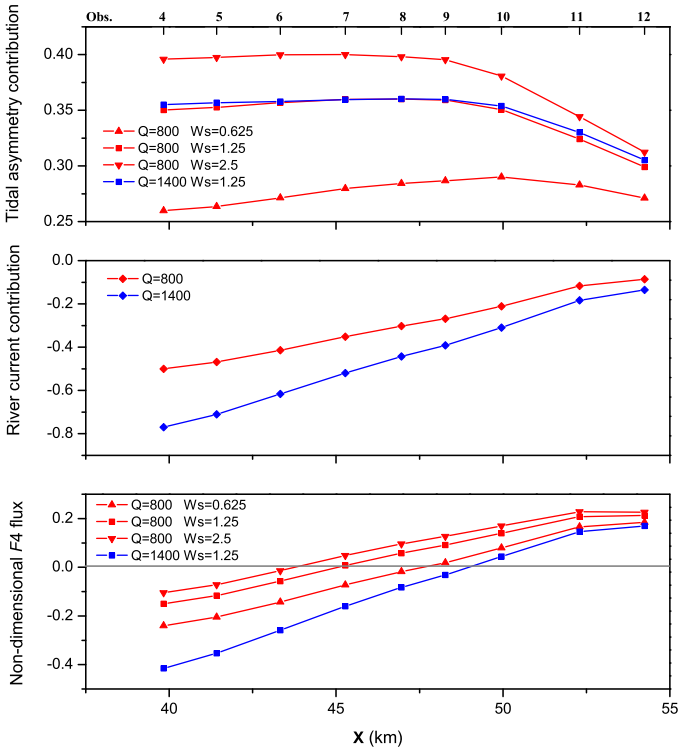

Figure 17. Nondimensional *F4* fluxes at points O4 to O12 based on equation (10). The river current and tidal asymmetry contributions are the first and second terms on the RHS of equation (10). Q is the river discharge (m^3/s), and W_s is the sediment settling velocity (mm/s).

The settling velocities modify the phase lags θ_ω and $\theta_{2\omega}$, and the river discharge causes different longitudinal distributions of u_0 and $(2\varphi_1-\varphi_2)$. Based on the above equation, the longitudinal dimensional *F4* distribution can be obtained using the harmonic constants $\hat{u}_0$, φ_1 and φ_2 at points O4 to O12 based on the 2-DH modeling (Figure 17). High river discharge pronouncedly intensifies the downstream flux induced by the river current (the first term on the RHS of equation (10)), but has little influences on the upstream flux induced by tidal asymmetry (the second term on the RHS of equation (10)). The low settling velocity, which is associated with large phase lags (θ_ω and $\theta_{2\omega}$) and more delayed response of SSC to velocity, results in a reduced upstream tidal asymmetry flux. Summarizing the two competing terms, the nondimensional *F4* fluxes show the negative (downstream) fluxes on the landward side and the positive (upstream) fluxes on the seaward side of the estuary. As a result, the associated flux convergences explain the mechanism of ETM formation. The zero-crossing points, which denote the core of the ETM, are located between points O6 and O7 for Q = 800 m^3/s and W_s = 2.5 mm/s, at O7 for Q = 800 m^3/s and W_s = 1.25 mm/s, at O9 for Q = 800 m^3/s and W_s = 0.625 mm/s, and between O9 and O10 for Q = 1400 m^3/s and W_s = 1.25 mm/s. These positions are consistent with the 2-DH modeling results (Figures 13 and 14). Thus, this simplified method successfully predicts the position of the ETM.

Using the harmonic constants of the estuarine barotropic tide based on the 2-DH modeling as input data, the analytical solutions for estuarine tides [e.g., *Friedrichs*, 2010] can, as a next step, be combined with the present sediment transport solutions to obtain the fully analytical prediction of ETM movement [*Prandle*, 2004].

6. Conclusion

Tidal pumping is shown to substantially contribute to ETM formation, especially in the case of well-mixed, macrotidal estuaries. It is demonstrated that the classical empirical decomposition method [*Dyer*, 1997] suggested for the analyzation of field observations may lead to erroneous results concerning the TPF and, hence, on conclusions about the mechanisms of ETM formation. This error is due to the effects of horizontal SSC gradients induced by advection and fine bed sediment supply. If these effects are excluded, the TPF clearly illustrates the convergence patterns and emphasizes its important role in the ETM formation. A simplified analytical expression suggests that the TPF is the result of the competition between the downstream flux induced by the river current and the sediment response lag and upstream flux induced by the tidal asymmetry and the lag. The field observations in the Yalu River estuary provide a typical example, where tidal pumping is identified as the dominant mechanism of ETM formation, and the position of the ETM for different river discharges and sediment settling velocities can be predicted by the concept of tidal pumping through numerical and analytical approaches.

© 2014. American Geophysical Union. All Rights Reserved.

Acknowledgments
The study was supported by the National Key Basic Research Project in China (2013CB956502), the Natural Science Foundation of China (NSFC 41306076, 41206070, 40976051), and the Natural Science Foundation of Jiangsu Province (BK2012316). We are grateful to Jing Zhang and Lixian Dong who organized the field work in 1994 and 1996. The observational and modeling data are available from the authors (QY) on request. The comments from two anonymous reviewers have substantially contributed to improving the clarity of the manuscript.

References

Allen, G. P., J. C. Salomon, P. Bassoullet, Y. Du Penhoat, and C. De Grandpre (1980), Effects of tides on mixing and suspended sediment transport in macrotidal estuaries, *Sedimentol. Geol.*, *26*, 69–90.

Amos, C. L., G. R. Daborn, H. A. Christian, A. Atkinson, and A. Robertson (1992), In situ measurements on fine-grained sediments from the Bay of Fundy, *Mar. Geol.*, *108*, 175–196.

Barua, D. K., S. A. Kuehl, R. L. Miller, and W. S. Moore (1994), Suspended sediment distribution and residual transport in the coastal ocean off the Ganges-Brahmaputra river mouth, *Mar. Geol.*, *120*, 41–61.

Bass, S. J., J. N. Aldridge, I. N. McCave, and C. E. Vincent (2002), Phase relationships between fine sediment suspensions and tidal currents in coastal seas, *J. Geophys. Res.*, *107*(C10), 3146, doi:10.1029/2001JC001269.

Becherer, J., H. Burchard, G. Floeser, V. Mohrholz, and L. Umlauf (2011), Evidence of tidal straining in well-mixed channel flow from microstructure observations, *Geophys. Res. Lett.*, *38*, L17611, doi:10.1029/2011GL049005.

Blair, N. E., and R. C. Aller (2012), The fate of terrestrial organic carbon in the marine environment, *Annu. Rev. Mar. Sci.*, *4*, 401–423.

Brenon, I., and P. Le Hir (1999), Modelling the turbidity maximum in the Seine Estuary (France): Identification of formation processes, *Estuarine Coastal Shelf Sci.*, *49*, 525–544.

Burchard, H., and H. Baumert (1998), The formation of estuarine turbidity maxima due to density effects in the salt wedge, *A hydrodynamic process study, J. Phys. Oceanogr.*, *28*, 309–321.

Burchard, H., and R. D. Hetland (2010), Quantifying the contributions of tidal straining and gravitational circulation to residual circulation in periodically stratified tidal estuaries, *J. Phys. Oceanogr.*, *40*, 1243–1262.

Cheng, P., and R. E. Wilson (2008), Modeling sediment suspensions in an Idealized tidal embayment: Importance of tidal asymmetry and settling lag, Estuaries Coasts, *31*, 828–842.

Cheng, P., M. Li, and Y. Li (2013), Generation of an estuarine sediment plume by a tropical storm, *J. Geophys. Res. Oceans*, *118*, 856–868, doi: 10.1002/jgrc.20070.

de Nijs, M. A. J., J. C. Winterwerp, and J. D. Pietrzak (2009), On harbour siltation in the fresh-salt water mixing region, *Cont. Shelf Res.*, *29*, 175–193.

de Nijs, M. A. J., J. C. Winterwerp, and J. D. Pietrzak (2010), The effects of the internal flow structure on SPM entrapment in the Rotterdam Waterway, *J. Phys. Oceanogr.*, *40*, 2357–2380.

Dronkers, J. (1986), Tide-induced residual transport of fine sediment, in *Physics of Shallow Bays and Estuaries*, pp. 228–244, Springer, Miami, Fla.

Dyer, K. R. (1997), *Estuaries—A Physical Introduction*, 2nd ed., 195 pp., John Wiley, Chichester, U. K.

Elliott, M., and A. K. Whitfield (2011), Challenging paradigms in estuarine ecology and management, *Estuarine Coastal Shelf Sci.*, *94*, 306–314.

Erikson, L. H., S. A. Wright, E. Elias, D. M. Hanes, D. H. Schoellhamer, and J. Largier (2013), The use of modeling and suspended sediment concentration measurements for quantifying net suspended sediment transport through a large tidally dominated inlet, *Mar. Geol.*, *345*, 96–112.

Festa, J. F., and D. V. Hansen (1976), A two-dimensional numerical model of estuarine circulation: The effects of altering depth and river discharge, *Estuarine Coastal Mar. Sci.*, *4*, 309–323.

Friedrichs, C. T. (2010), Barotropic tides in channelized estuaries, in *Contemporary Issues in Estuarine Physics*, edited by A. Valle-Levinson, pp. 27–61, Cambridge Univ. Press, Cambridge, U. K.

Friedrichs, C. T., B. A. Armbrust, and H. E. de Swart (1998), Hydrodynamics and equilibrium sediment dynamics of shallow, funnel-shaped tidal estuaries, in *Physics of Estuaries and Coastal Seas*, edited by J. Dronkers and M. Scheffers, pp. 315–328, A. A. Balkema, Rotterdam, Netherlands.

Ganju, N. K., D. H. Schoellhamer, and B. A. Bergamaschi (2005), Suspended sediment fluxes in a tidal wetland: Controlling factors, and error analysis, *Estuaries*, *28*, 812–822.

Gao, J. H., S. Gao, Y. Cheng, L. X. Dong, and J. Zhang (2004), Formation of turbidity maxima in the Yalu River estuary, China, *J. Coastal Res.*, *43*(SI), 134–146.

Gao, J. H., J. Li, H. Wang, F. L. Bai, Y. Cheng, and Y. P. Wang (2012), Rapid changes of sediment dynamic processes in Yalu River Estuary under anthropogenic impacts, *Int. J. Sediment Res.*, *27*, 37–49.

Garnier, J., G. Billen, J. Némery, and M. Sebilo (2010), Transformations of nutrients (N, P, Si) in the turbidity maximum zone of the Seine estuary and export to the sea, *Estuarine Coastal Shelf Sci.*, *90*, 129–141.

Gelfenbaum, G. (1983), Suspended-sediment response to semidiunal and forthightly tidal variations in mesotidal estuary: Columbia River, USA, *Mar. Geol.*, *52*, 39–57.

Geyer, W. R., R. Signell, and G. Kineke (1998), Lateral trapping of sediment in a partially mixed estuary, in *Physics of Estuaries and Coastal Seas*, edited by J. Donkers and M. Sheffers, pp. 115–124, A. A. Balkema, Rotterdam, Netherlands.

Gong, W. P., L. W. Jia, J. Shen, and J. T. Liu (2014), Sediment transport in response to changes in river discharge and tidal mixing in a funnel-shaped micro-tidal estuary, *Cont. Shelf Res.*, *76*, 89–107.

Grabemann, I., and G. Krause (1989), Transport processes of suspended matter derived from time series in a tidal estuary, *J. Geophys. Res.*, *94*, 14,373–14,379.

Grabemann, I., R. J. Uncles, G. Krause, and J. A. Stephens (1997), Behaviour of turbidity maxima in the Tamar (U.K.) and Weser (F.R.G.) estuaries, *Estuarine Coastal Shelf Sci.*, *45*, 235–246.

Green, M. O., R. G. Bell, T. J. Dolphin, and A. Swales (2000), Silt and sand transport in a deep tidal channel of a large estuary (Manukau Harbour, New Zealand), *Mar. Geol.*, *163*, 217–240.

Herman, P. M. J., and C. H. R. Heip (1999), Biogeochemistry of the MAximum TURbidity Zone of Estuaries (MATURE): Some conclusions, *J. Mar. Syst.*, *22*, 89–104.

Hibma, A., H. M. Schuttelaars, and Z. B. Wang (2003), Comparison of longitudinal equilibrium profiles of estuaries in idealized and process-based models, *Ocean Dyn.*, *53*, 252–269.

Islam, M. S., M. Hibino, and M. Tanaka (2006), Distribution and diets of larval and juvenile fishes: Influence of salinity gradient and turbidity maximum in a temperate estuary in upper Ariake Bay, Japan, *Estuarine Coastal Shelf Sci.*, *68*, 62–74.

Jago, C. K., A. K. Ishak, S. E. Jones, and M. R. G. Goff (2006), An ephemeral turbidity maximum generated by resuspension of organic-rich matter in a macrotidal estuary, S.W. Wales, *Estuaries Coasts*, *29*, 197–208.

Jay, D. A., and J. D. Musiak (1994), Particle trapping in estuarine tidal flows, *J. Geophys. Res.*, *99*, 20,445–20,461.

Jay, D. A., W. R. Geyer, R. J. Uncles, J. Vallino, J. Largier, and W. R. Boynton (1997), A review of recent developments in estuarine scalar flux estimation, *Estuaries*, *20*, 262–280.

Kappenberg, J., and I. Grabemann (2001), Variability of the mixing zones and estuarine turbidity maxima in the Elbe and Weser estuaries, *Estuaries*, *24*, 699–706.

 © 2014. American Geophysical Union. All Rights Reserved.

Kim, Y. H., and G. Voulgaris (2008), Lateral circulation and suspended sediment transport in a curved estuarine channel: Winyah Bay, SC, USA, *J. Geophys. Res.*, *113*, C09006, doi:10.1029/2007JC004509.
Le Hir, P., A. Ficht, R. S. Jacinto, P. Lesueur, J.-P. Dupont, R. Lafite, I. Brenon, B. Thouvenin, and P. Cugier (2001), Fine sediment transport and accumulations at the mouth of the Seine Estuary (France), *Estuaries*, *24*, 950–963.
Lefebvre, J.-P., S. Ouillon, V. D. Vinh, D. Arfi, J.-Y. Panché, X. Mari, C. V. Thuoc, and J.-P. Torréton (2012), Seasonal variability of cohesive sediment aggregation in the Bach Dang–Cam Estuary, Haiphong (Vietnam), *Geo Mar. Lett.*, *32*, 103–121.
Lesser, G. R., J. A. Roelvink, J. A. T. M. van Kesteren, and G. S. Stelling (2004), Development and validation of a three-dimensional morphological model, *Coastal Eng.*, *51*, 883–915.
Li, J., and Z. Chen (1998), Sediment resuspension and implications for turbidity maximum in the Changjiang Estuary, *Mar. Geol.*, *148*, 117–124.
Partheniades, E. (1965), Erosion and deposition of cohesive soil, *J. Hydraul. Div.*, *91*, 105–139.
Pino, Q. M., G. M. E. Perillo, and P. Santamarina (1994), Residual fluxed in a cross-section of the Valdivia River Estuary, Chile, *Estuarine Coastal Shelf Sci.*, *38*, 491–505.
Postma, H. (1967), Sediment transport and sedimentation in the estuarine environment, in *Estuaries*, edited by G. H. Lauff, pp. 158–179, Am. Assoc. for the Adv. of Sci., Washington, D. C.
Prandle, D. (2004), Sediment trapping, turbidity maxima, and bathymetric stability in macrotidal estuaries, *J. Geophys. Res.*, *109*, C08001, doi:10.1029/2004JC002271.
Pritchard, D. W. (1956), The dynamic structure of a coastal plane estuary, *J. Mar. Res.*, *15*, 33–42.
Sanford, L. P., and J. P. Halka (1993), Assessing the paradigm of mutually exclusive erosion and deposition of mud, with examples from upper Chesapeake Bay, *Mar. Geol.*, *114*, 37–57.
Sanford, L. P., S. E. Suttles, and J. P. Halka (2001), Reconsidering the physics of the Chesapeake Bay estuarine turbidity maximum, *Estuaries*, *24*, 655–669.
Schoellhamer, D. H. (1996), Factors affecting suspended-solids concentrations in South San Francisco Bay, California, *J. Geophys. Res.*, *101*, 12,087–12,095.
Shi, Y., J. H. Gao, Y. Yang, L. J. Ran, F. X. Li, Y. Liu, and Y. Cheng (2013), Responses of depositional characteristics of tidal flats on the west bank of the Yalu River estuary to catchment changes [in Chinese with English abstract], *Quat. Sci.*, *32*, 1221−1233.
Simpson, J. H., J. Brown, J. Matthews, and G. Allen (1990), Tidal straining, density currents, and stirring in the control of estuarine stratification, *Estuaries*, *13*, 125–132.
Soulsby, R. L. (1997), *Dynamics of Marine Sands*, 249 pp., Thomas Telford, Oxford, U. K.
Stanev, E. V., G. Brink-Spalink, and J.-O. Wolff (2007), Sediment dynamics in tidally dominated environments controlled by transport and turbulence: A case study for the East Frisian Wadden Sea, J. Geophys. Res., *112*, C04018, doi: 10.1029/2005JC003045.
State Oceanic Administration (1998), *Chinese Harbours and Embayments, Important Estuaries* [in Chinese], vol. 14, pp. 386–432, Ocean Press, Beijing.
Su, J. L., and K. S. Wang (1986), The suspended sediment balance in Changjiang estuary, *Estuarine Coastal Shelf Sci.*, *23*, 81–98.
Temmerman, S., T. J. Bouma, G. Govers, Z. B. Wang, M. B. De Vries, and P. M. J. Herman (2005), Impact of vegetation on flow routing and sedimentation patterns: Three-dimensional modeling for a tidal marsh, *J. Geophys. Res.*, *110*, F04019, doi:10.1029/2005JF000301.
Uncles, R. J., and J. A. Stephens (1989), Distributions of suspended sediment at high water in a macrotidal estuary, *J. Geophys. Res.*, *94*, 14,395–14,405.
Uncles, R. J., and J. A. Stephens (1993), The freshwater-saltwater interface and its relationship to the turbidity maximum in the Tamar Estuary, United Kingdom, *Estuaries*, *16*, 126–141.
Uncles, R. J., R. C. A. Elliott, and S. A. Weston (1985a), Dispersion of salt and suspended sediment in a partly mixed estuary, *Estuaries*, *8*, 256–269.
Uncles, R. J., R. C. A. Elliott, and S. A. Weston (1985b), Observed fluxes of water, salt and suspended sediment in a partly mixed estuary, *Estuarine Coastal Shelf Sci.*, *20*, 147–167.
van der Wegen, M., and J. A. Roelvink (2008), Long-term morphodynamic evolution of a tidal embayment using a two-dimensional, process-based model, *J. Geophys. Res.*, *113*, C03016, doi:10.1029/2006JC003983.
van Leussen, W. (1991), Fine sediment transport under tidal action, *Geo Mar. Lett.*, *11*, 119–126.
van Maren, D. S., S. C. Liew, and G. M. Jahid Hasan (2014), The role of terrestrial sediment on turbidity near Singapore's coral reefs, *Cont. Shelf Res.*, *76*, 75–88.
van Rijn, L. C. (2000), General view on sand transport by currents and waves, *Rep. Z2899.20-Z2099.30-Z2824.30*, Delft Hydraul., Delft, Netherlands.
Wang, Y., Q. Yu, and S. Gao (2014), Modeling interrelationships between morphological evolution and grain-size trends in back-barrier tidal basins of the East Frisian Wadden Sea, *Geo Mar. Lett.*, *34*, 37–49.
Wang, Y. P., G. Voulgaris, Y. Li, Y. Yang, J. Gao, J. Chen, and S. Gao (2013), Sediment resuspension, flocculation, and settling in a macrotidal estuary, *J. Geophys. Res. Oceans*, *118*, 5591–5608, doi:10.1002/jgrc.20340.
Wellershaus, S. (1981), Turbidity maximum and shoaling in the Weser estuary, *Arch. Hydrobiol.*, *92*, 161–198.
Wells, J. T. (1995), Tide-dominated estuaries and tidal rivers, in *Geomorphology and Sedimentology of Estuaries, Developments in Sedimentology*, vol. 53, 2nd ed., edited by G. M. E. Perillo, pp. 179–205, Elsevier Sci., Amsterdam.
Whitehouse, R., R. Soulsby, W. Roberts, and H. Mitchener (2000), *Dynamics of Estuarine Mud*, 210 pp., Thomas Telford, London, U. K.
Winterwerp, J. C. (1983), Decomposition of the mass transport in narrow estuaries, *Estuarine Coastal Shelf Sci.*, *16*, 627–638.
Winterwerp, J. C., and W. G. M. van Kestern (2004), *Introduction to the Physics of Cohesive Sediments in the Marine Environment*, 466 pp., Elsevier, Amsterdam.
Xie, D., Z. B. Wang, S. Gao, and H. J. de Vriend (2009), Modeling the tidal channel morphodynamics in a macro-tidal embayment, Hangzhou Bay, China, *Cont. Shelf Res.*, *29*, 1757–1767.
Xu, F., D.-P. Wang, and N. Riemer (2010), An idealized model study of flocculation on sediment trapping in an estuarine turbidity maximum, *Cont. Shelf Res.*, *30*, 1314–1323.
Yu, Q., B. Flemming, and S. Gao (2011), Tide-induced vertical suspended sediment concentration profiles: Phase lag and amplitude attenuation, *Ocean Dyn.*, *61*, 403–410.
Yu, Q., Y. P. Wang, B. W. Flemming, and S. Gao (2012a), Tide-induced suspended sediment transport: Depth-averaged concentrations and horizontal residual fluxes, *Cont. Shelf Res.*, *34*, 53–63.
Yu, Q., Y. W. Wang, S. Gao, and B. W. Flemming (2012b), Modeling the formation of a sand bar within a large funnel-shaped, tide-dominated estuary: Qiantangjiang Estuary, China, *Mar. Geol.*, *299–302*, 63–76.

© 2014. American Geophysical Union. All Rights Reserved.